High-resolution marine data and transient simulations support orbital forcing of ENSO amplitude since the mid-Holocene

Quaternary Science Reviews 268 (2021) 107125

Contents lists available at ScienceDirect

Quaternary Science Reviews

journal homepage: www.elsevier.com/locate/quascirev

High-resolution marine data and transient simulations support orbital forcing of ENSO amplitude since the mid-Holocene

Matthieu Carré [a, b, *], Pascale Braconnot [c], Mary Elliot [d], Roberta d'Agostino [e], Andrew Schurer [f], Xiaoxu Shi [g], Olivier Marti [c], Gerrit Lohmann [g, h], Johann Jungclaus [e], Rachid Cheddadi [i], Isma Abdelkader di Carlo [c], Jorge Cardich [b], Diana Ochoa [b], Rodolfo Salas Gismondi [b], Alexander Pérez [b], Pedro E. Romero [b], Bruno Turcq [a], Thierry Corrège [j], Sandy P. Harrison [k]

[a] IPSL-LOCEAN Laboratory (UMR7159 CNRS-IRD-MNHN-Sorbonne Universités), Paris, France
[b] Facultad de Ciencias y Filosofía, LID, CIDIS, Universidad Peruana Cayetano Heredia, Lima, Peru
[c] Laboratoire des Sciences du Climat et de l'Environnement-IPSL, Unité Mixte CEA-CNRS-UVSQ, Université Paris-Saclay, Orme des Merisiers, Gif-sur-Yvette, France
[d] LPG, Université de Nantes, France
[e] Max Planck Institute for Meteorology, Hamburg, Germany
[f] School of Geosciences, University of Edinburgh, UK
[g] Alfred Wegener Institute, Helmholtz Centre for Polar and Marine Research, Bremerhaven, Germany
[h] Department of Environmental Physics & MARUM, University of Bremen, Bremen, Germany
[i] Institut des Sciences de l'Evolution de Montpellier, University of Montpellier, CNRS, IRD, Montpellier, France
[j] Université de Bordeaux, UMR 'EPOC' CNRS 5805, Pessac, France
[k] Department of Geography and Environmental Science, University of Reading, Reading, RG6 6AB, UK

ARTICLE INFO

Article history:
Received 13 April 2021
Received in revised form
13 July 2021
Accepted 25 July 2021
Available online 20 August 2021

Handling Editor: I. Hendy

Keywords:
El niño southern oscillation
Holocene
Earth system models
Insolation
Corals
Bivalves
Tropical pacific

ABSTRACT

Lack of constraint on spatial and long-term temporal variability of the El Niño southern Oscillation (ENSO) and its sensitivity to external forcing limit our ability to evaluate climate models and ENSO future projections. Current knowledge of Holocene ENSO variability derived from paleoclimate reconstructions does not separate the role of insolation forcing from internal climate variability. Using an updated synthesis of coral and bivalve monthly resolved records, we build composite records of seasonality and interannual variability in four regions of the tropical Pacific: Eastern Pacific (EP), Central Pacific (CP), Western Pacific (WP) and South West Pacific (SWP). An analysis of the uncertainties due to the sampling of chaotic multidecadal to centennial variability by short records allows for an objective comparison with transient simulations (mid-Holocene to present) performed using four different Earth System models. Sea surface temperature and pseudo-$\delta^{18}O$ are used in model-data comparisons to assess the potential influence of hydroclimate change on records. We confirm the significance of the Holocene ENSO minimum (HEM) 3-6ka compared to low frequency unforced modulation of ENSO, with a reduction of ENSO variance of ~50 % in EP and ~80 % in CP. The approach suggests that the increasing trend of ENSO since 6ka can be attributed to insolation, while models underestimate ENSO sensitivity to orbital forcing by a factor of 4.7 compared to data, even when accounting for the large multidecadal variability. Precession-induced change in seasonal temperature range is positively linked to ENSO variance in EP and to a lesser extent in other regions, in both models and observations. Our regional approach yields insights into the past spatial expression of ENSO across the tropical Pacific. In the SWP, today under the influence of the South Pacific Convergence Zone (SPCZ), interannual variability was increased by ~200 % during the HEM, indicating that SPCZ variability is independent from ENSO on millennial time scales.

1. Introduction

Defining the natural variability of the El Niño southern

* Corresponding author. IPSL-LOCEAN Laboratory (UMR7159 CNRS-IRD-MNHN-Sorbonne Universités), Paris, France.
E-mail address: matthieu.carre@locean.ipsl.fr (M. Carré).

https://doi.org/10.1016/j.quascirev.2021.107125

Oscillation (ENSO) and estimating its sensitivity to external climate forcings is a fundamental requirement to produce reliable projections of ENSO activity under future climate change (Brown et al., 2008a, 2008b; Schmidt et al., 2014). Paleoclimate archives provide the only means to test current climate models and their simulations of ENSO under different global climate states (Braconnot et al., 2012a; Harrison et al., 2015; Emile-Geay et al., 2020). The Holocene (past 11,700 years) provides an ideal period to study the effects of changes in seasonal insolation due to orbital precession, which induced large climatic changes in the tropics (Kutzbach, 1981; Joussaume et al., 1999; Haug et al., 2001). Reduced ENSO activity, i.e., weaker events and reduced interannnual variability compared to modern times, is usually found in mid-Holocene time-slice simulations from the Paleomodelling Intercomparison Project (PMIP) across different phases (Otto-Bliesner, 1999; Clement et al., 2000; Liu et al., 2000; J. R. Brown et al., 2008; Zheng et al., 2008; Braconnot et al., 2012b; Luan et al., 2012; Emile-Geay et al., 2016; Brown et al., 2020; An and Choi, 2014; Masson-Delmotte et al., 2013). The ENSO activity is significantly suppressed in the PMIP2, and marginally reduced in the PMIP3/4, with most of the models ranging between 0 and 20 % decreased variability for the conventional El Niño (Brown et al., 2020). The mid-Holocene reduction of ENSO activity is currently underestimated by climate models compared to paleoclimate reconstructions (Emile-Geay et al., 2016).

Despite a qualitative agreement of models with a number of paleoclimate records, a detailed data-model assessment is hindered by differences between different types of records and uncertainties in their interpretation (Brown et al., 2008a, 2008b). Minimum ENSO activity in the Holocene is observed in the early Holocene in some records (Conroy et al., 2008; Moy et al., 2002; Rodbell et al., 1999; Tudhope et al., 2001) and in the 3-6ka period in others (Carré et al., 2014; Chen et al., 2016; Koutavas and Joanides, 2012; Zhang et al., 2014). The apparent delay between the time of minimum ENSO variability and what would be expected from insolation forcing raises the question whether observed change in ENSO during the Holocene was actually significant (forced) compared to the large internal (unforced) variability of ENSO (Cobb et al., 2013). A robust assessment of the signal to noise ratio in palaeo-records and in climate simulations is required to test whether ENSO has been affected by orbital forcing during the Holocene as previously suggested (Clement et al, 1999, 2000, 1999; Moy et al., 2002) or if the observed changes are a stochastic result of unforced variability (Cobb et al., 2013).

The lack of convergence between paleoclimate reconstructions arises for three reasons: differences in the climate variables proxies are sensitive to, record location, and the time resolution of the records. First, paleoclimate records relate, more or less directly, separately or in combination, to a variety of climate variables including sea surface temperature (SST), thermocline temperature, air temperature, local precipitation, sediment transport, hydrological budget (P-E), upwelled nutrients, oxygenation. These climate variables reflect different facets of ENSO that may have evolved in different ways, spatially and temporally. It is likely that atmospheric teleconnections that determine the relationship between Pacific SST anomalies and continental rainfall anomalies have evolved during the Holocene (Braconnot et al., 2019a; Crétat et al., 2020), given the more northerly position of the boreal summer Intertropical convergence zone (ITCZ) (Haug et al., 2001; Sachs et al., 2018; Yan et al., 2015), and the strengthened northern hemisphere (D'Agostino et al., 2019; Goodbred and Kuehl, 2000; Joussaume et al., 1999; Wang et al., 2005) and weakened southern hemisphere (Cruz et al., 2009; Mollier-Vogel et al., 2013; D'Agostino et al., 2020) monsoons during the mid-Holocene. This means that the ability of rainfall-related records (generally located on continents) to document Pacific SST anomalies and their amplitude has also likely evolved through the Holocene. Secondly, changes in ENSO activity are inferred from records retrieved in very distant regions including Africa, the Indo Pacific Warm Pool, the South-West Pacific, the Central Pacific, the Eastern Pacific, North, central and south America. ENSO is not unidimensional so that its characteristics may change unevenly across the Pacific. It involves at least two spatial modes of variability (flavours), the Central Pacific (C) and Eastern Pacific (E) modes, defined by the location of the maximum SST anomaly in the Equatorial Pacific and associated with different teleconnection patterns (Ashok et al., 2007; Kao and Yu, 2009; Sulca et al., 2018; Takahashi et al., 2011). The frequency and amplitude of these flavours have evolved in the past decades (Dewitte et al., 2012; Lee and McPhaden, 2010) and may evolve in the future (Yeh et al., 2009). For example, the 2015–16 El Niño event, one of the strongest in the instrumental record, produced relatively mild SST anomalies in Peru, while the 2017 El Niño event devastated the Peruvian coast (Echevin et al., 2018; Garreaud, 2019; Rodríguez-Morata et al., 2019) without producing any anomaly in the Western tropical Pacific. It is thus clear that past changes in ENSO flavours could potentially account for large differences in paleo-ENSO records around the Pacific Ocean (Karamperidou et al., 2015). Finally, differences in interpretation of the paleoclimate records arise from differences in their length and resolution. In low resolution paleoclimate records that do not resolve individual ENSO events, inferences about ENSO activity are limited to speculations assuming that changes in mean conditions result from changes in the statistics of ENSO events (Shulmeister and Lees, 1995).

In this paper, we present quantitative composite records of SST seasonality and interannual variability changes over the Holocene for four regions of the tropical Pacific, based on an update of the synthesis of coral and bivalve $\delta^{18}O$ records made by Emile-Geay et al. (2016) and including Sr/Ca records. These archives provide the most direct and reliable observations of ENSO-related climate variability and thus minimize archive-related discrepancies (Beck et al., 1992; Cole et al., 1993; Welsh et al., 2011; Carré et al., 2013; Driscoll et al., 2014). The composite records include an estimation of uncertainties related to the records and to their sampling of the unforced decadal to multi-centennial climatic variability. Since the four regions provide an adequate representation of the spatial pattern of Holocene paleoclimatic changes, we can assess the spatial dimension of ENSO variability changes and its relationship with climate seasonality. We assume that interannual to decadal variability (2–9 years) in the equatorial Pacific is associated with ENSO or to the different characteristics of El-Niño and La-Niña events, although we acknowledge that the variability in the South West Pacific might be affected by other factors (Saint-Lu et al., 2015). We compare these reconstructions with four transient simulations from the middle Holocene to present made with the IPSL-CM5 (Braconnot et al., 2019a), IPSL-CM6 (Braconnot et al., 2019b), AWI (Sidorenko et al., 2019), and MPI (Bader et al., 2020; Dallmeyer et al., 2020) Earth system models (ESMs). These are state of the art models equivalent in terms of complexity and performances to models performing PMIP3-CMIP5 simulations (Braconnot et al., 2012a; Taylor et al., 2012) used as references in the IPCC AR5 report (Stocker et al., 2013). They all reproduce ENSO-type variability, and share the common model biases, such as the erosion of the warm pool, and ENSO anomalies slightly shifted to the center of the Pacific basin with a too limited meridional extension compared to observations (Bellenger et al., 2014). Transient simulations offer a representation of climate under the more realistic conditions of continuously changing external forcing and provide a more robust representation of centennial to millennial internal variability in models than equilibrium simulations (Wittenberg, 2009). Model-data comparisons use both SSTs and pseudo-aragonite $\delta^{18}O$ values from model transient simulations, following

the approach of Emile-Geay et al. (2016) since the spatial gradients and temporal changes in the relative contribution of SST and water $\delta^{18}O$ variability in carbonate $\delta^{18}O$ records could be a source of bias in the records of past ENSO (Thompson et al., 2011; Russon et al., 2013; Stevenson et al., 2013, 2018; Conroy et al., 2017). We evaluate to what extent climate simulations are consistent with observations considering uncertainties and the range of internal unforced variability of ENSO, and whether a detectable effect of the orbital forcing on ENSO emerges from the unforced internal variability.

The paleoclimate synthesis and the transient simulations are presented in section 2. The construction of the composite records, the estimation of uncertainty, and the model-data comparison are presented in section 3. Section 4 examines the observed and simulated changes in seasonality and interannual variability and the detection-attribution of the insolation forcing. We use simulations and observations together in section 5 to discuss the role of insolation in the Holocene history of ENSO, spatial changes in ENSO, the relationship between ENSO and the annual cycle, and with the South Pacific Convergence zone (SPCZ).

2. Datasets

2.1. Data synthesis

The paleoclimate data synthesis used in this study was extracted from the publicly available PACMEDY Coral&Bivalve database_v1 which gathers fossil coral and bivalve high resolution geochemical records of the Holocene and late glacial period (Carré et al., 2021). The synthesis includes Sr/Ca and isotopic ($\delta^{18}O$) records from fossil corals and bivalves from the tropical Pacific that meet the following criteria:

(1) the fossil record is dated to some interval in the past 10,000 years,
(2) the temporal resolution of the fossil record is at least 3 months,
(3) there is a modern record at least 15 years long obtained from the same species in the same locality.

73 coral and bivalve records from the tropical Pacific were retrieved from public repositories or provided by the authors (Table 1). We do not include microatoll records, which are thought to reflect conditions of the lagoon instead of the open ocean. Sr/Ca records were included. Annually resolved records (or lower resolution) were not included because of the focus on seasonality in this study and potential seasonal biases in low resolution records (Carré and Cheddadi, 2017). Sr/Ca and $\delta^{18}O$ records obtained from the same coral are considered as different records. The Eastern tropical Pacific records are groups of short-lived bivalve shells from the same deposit (Carré et al., 2014).

All datasets have been previously published (Table 1). A few of the datasets were digitised from published figures when the original data files were unavailable. All datasets were interpolated to a constant time resolution (1 month or 3 months depending on the original resolution). We used the published interpolated data when available, and linear interpolation of the raw data using seasonal extrema as anchor points when not. Most records have a monthly resolution. Radiometric dates were assumed to correspond to the middle of the coral records unless otherwise indicated in the publications. Fossil records from the Australian Great Barrier Reef were not included because of the lack of modern reference records.

The records were grouped in four regions (Fig. 1a), defined as follows:

Eastern Pacific (EP): from 20°S to 8°S; from 278°E to 290°E
Central Pacific (CP): from 0°N to 8°N; from 194°E to 206°E
Western Pacific (WP): from 10°S to 2°S; from 142°E to 152°E
South West Pacific (SWP): from 24°S to 14°S; from 160°E to 172°E

The fossil records represent a total of 1964 years out of the last 10,000 years. The distribution of data in time and space is heterogeneous (Fig. 1b). Two thirds of the data are from the CP with 1312 years recorded. Both numbers of records and length of time covered are lower in other regions: EP (214 years), WP (245 years), and SWP (443 years). The CP box partially overlaps with the Niño3.4 box. Located in the northern hemisphere, these records may be sensitive to the northward extent of La Niña and El Niño anomalies. No data are available from the Niño3 or the Niño1+2 box. The data are most abundant for the last millennium and the mid-to late Holocene (7–6 and 5–3 ka). The abundance in the mid- and late Holocene reflects the accessibility of emerged fossil reefs in the CP and SWP regions as a result of the mid-Holocene sea-level highstand (Grossman et al., 1998; Lambeck and Nakada, 1990; Pirazzoli and Montaggioni, 1988; Woodroffe and Horton, 2005). The data minimum between 5 and 6 ka in all regions cannot be explained except as a random sampling effect. The lack of observations between 2 and 1 ka probably reflects reduced sampling effort and insufficient tectonic uplift to expose fossils, while the comparative lack before 7ka is likely due to lower sea-level so that most fossils of this period are underwater today. Early Holocene records are available in Papua New Guinea and Vanuatu because rapid tectonic uplift has led to the emergence of fossil reefs (Beck et al., 1997; Chappell and Polach, 1991; Corrège et al., 2004; McCulloch et al., 1996; Tudhope et al., 2001). Early Holocene records from Peru are available from anthropogenic shell mounds in archaeological sites (Carré et al, 2005b, 2013, 2014; Lavallée et al., 2011; Sandweiss et al., 1998, 2020).

Although corals and mollusks have been shown to reflect temperature variability and ENSO, they also have limitations. Since the records are located in coastal regions, they may be affected by local environmental heterogeneity. Furthermore, these organisms stop growing or die if temperature or salinity physiological thresholds are exceeded, which may occur during extraordinary El Niño events (Arntz et al., 1987; Glynn et al., 2001; Vargas-Ángel et al., 2019).

2.2. Climate model simulations

We used four transient simulations from climate models IPSL-CM5, IPSL-CM6, AWI-ESM2, MPI-ESM (Table 2). The four experiments were forced by evolving orbital parameters calculated according to (Berger, 1978), as proposed for PMIP4 transient simulations (Otto-Bliesner et al., 2017). Greenhouse gas (GHG) concentration is prescribed following the PMIP4 protocol (Otto-Bliesner et al., 2017) in IPSL-CM5 and IPSL-CM6 simulations, ice cores records from Köhler et al. (2017) for the AWI-ESM2 simulation, and updated ice core data for the MPI-ESM simulation (Dallmeyer et al., 2020). The small differences in GHG forcing are not expected to influence the results.

2.2.1. Description of the IPSL-CM5 simulation

The IPSL-CM5 simulation was performed with an updated version of the IPSLCM5A-LR model used for PMIP3-CMIP5 (Dufresne et al., 2013; Kageyama et al., 2013) with improved climatology and computing performance (Sepulchre et al., 2020). Sea ice is run at the ocean horizontal resolution and land surface at the atmospheric horizontal resolution. The carbon cycle over land and ocean is fully interactive. However, atmospheric CO_2 concentration is prescribed and pre-industrial vegetation cover is used

Table 1
Metadata of mollusk and coral records from the Pacific used in this study. Shaded records indicate modern records used as reference for $\delta^{18}O$ (blue), Sr/Ca (yellow), or both (green) for the following unshaded fossil records. The $\delta^{18}O$ (Sr) column shows 1 if the archive yielded a $\delta^{18}O$ (Sr/Ca) record, and 0 if not. Archives are grouped by proxy regions (SWP, WP, CP, EP) as defined in section 2.1 (Cobb et al., 2003; DeLong et al., 2013; Kilbourne et al., 2004; Montaggioni et al., 2006; Stephans et al., 2004; McGregor H. et al. (2013)).

Site	Archive code	genus	lon (°E)	lat (°N)	Age (Cal Yr BP)	Res. (month)	Record length (years)	$\delta^{18}O$	Sr	Reference
SWP										
Amédée L.	Stack4	*Porites*	166,47	-22,48	-17±0	1	26	1	0	Stephans et al. (2004)
Amédée L.	mean	*Porites*	166,47	-22,48	301±0	1	350	0	1	DeLong et al. (2013)
Bayes Islet	Bayes 1	*Porites*	165,48	-20,90	3990±145	1	49	1	1	Emile-Geay et al. (2016)
Naia Bay	Naia5.5	*Porites*	166,25	-22,16	5508±68	1	20	1	1	Lazareth et al. (2013)
Vata Ricaudy	Vata_1	*Porites*	166,45	-22,31	6090±90	1	4	0	1	Montaggioni et al. (2006)
Vata Ricaudy	Vata_2	*Porites*	166,45	-22,31	6210±120	1	3	0	1	Montaggioni et al. (2006)
Vata Ricaudy	Vata_3	*Porites*	166,45	-22,31	6330±110	1	8	0	1	Montaggioni et al. (2006)
Espiritu Santo	04vanu01a	*Porites*	167,20	-15,70	22±0	1	65	1	1	Kilbourne et al. (2004)
Tasmalum	9A	*Porites*	166,90	-15,61	4175±15	1	47	0	1	Corrège et al. (2000)
Espiritu Santo	Psp-06-09	*Porites*	167,18	-15,35	6610±121	1	26	1	1	Duprey et al. (2012)
Espiritu Santo	Psp-07-09	*Porites*	167,18	-15,35	6662±96	1	20	1	1	Duprey et al. (2012)
Espiritu Santo	Beck97-4	*Porites*	167,18	-15,35	4166±15	1	6	0	1	Beck et al. (1997)
Espiritu Santo	Beck97-3	*Porites*	167,18	-15,35	9509±26	1	5	0	1	Beck et al. (1997)
Espiritu Santo	Beck97-2	*Porites*	167,18	-15,35	9688±27	1	5	0	1	Beck et al. (1997)
WP										
Madang	DT91-7	*Porites*	145,82	-5,22	70±0	3	113	1	0	Tudhope et al. (2001)
Madang	M93TBFC	*Porites*	145,82	-5,22	2500±400	3	40	1	0	Tudhope et al. (2001)
Laing Island	LaingFC2	*Porites*	144,88	-4,15	2700±500	3	95	1	0	Tudhope et al. (2001)
Huon Peninsula	H95-16	*Porites*	147,60	-6,12	6500±70	3	49	1	0	Tudhope et al. (2001)
Huon Peninsula	MT03-7	*Tridacna*	147,62	-6,13	-36±0	1	16	1	0	Welsh et al. (2011)
Huon Peninsula	T58	*Tridacna*	147,62	-6,13	8090±150	1	18	1	0	Driscoll et al. (2014)
Huon Peninsula	T73	*Tridacna*	147,62	-6,13	7280±150	1	20	1	0	Driscoll et al., (2014)
Huon Peninsula	T75	*Tridacna*	147,62	-6,13	8760±460	1	12	1	0	Driscoll et al., (2014)
Huon Peninsula	HU	*Porites*	147,71	-6,27	-29±0	1	9	0	1	McCulloch et al. (1996)
Huon Peninsula	BBU7	*Porites*	147,78	-6,31	8920±60	1	5	0	1	McCulloch et al., (1996)
Huon Peninsula	BS1	*Porites*	147,78	-6,31	7370±50	1	6	0	1	McCulloch et al., (1996)
CP										
Palmyra	modern	*Porites*	-162,10	5,88	64±5	1	112	1	0	Cobb et al. (2003)
Palmyra	sb13	*Porites*	-162,10	5,88	296±5	1	42	1	0	Cobb et al. (2003)
Palmyra	sb6	*Porites*	-162,10	5,88	538±5	1	31	1	0	Cobb et al. (2003)
Palmyra	sb5	*Porites*	-162,10	5,88	545±5	1	43	1	0	Cobb et al. (2003)
Palmyra	sb7	*Porites*	-162,10	5,88	623±5	1	31	1	0	Cobb et al. (2003)
Palmyra	sb17	*Porites*	-162,10	5,88	801±5	1	71	1	0	Cobb et al. (2003)

Palmyra	nb12	*Porites*	-162,10	5,88	1022±5	1	33	1	0	Cobb et al. (2003)
Palmyra	spl14	*Porites*	-162,10	5,88	633±5	1	147	1	0	Cobb et al. (2003)
Palmyra	spl17	*Porites*	-162,10	5,88	315±5	1	68	1	0	Cobb et al. (2003)
Fanning	fann_mod_spl	*Porites*	-159,35	3,85	0±0	1	56	1	0	Cobb et al. (2013)
Fanning	v10	*Porites*	-159,35	3,85	3075±12	1	81	1	0	Cobb et al. (2013)
Fanning	v30	*Porites*	-159,35	3,85	5999±13	1	41	1	0	Cobb et al. (2013)
Fanning	v13	*Porites*	-159,35	3,85	6033±12	1	26	1	0	Cobb et al. (2013)
Fanning	v8	*Porites*	-159,35	3,85	6097±18	1	41	1	0	Cobb et al. (2013)
Fanning	v28	*Porites*	-159,35	3,85	6360±13	1	20	1	0	Cobb et al. (2013)
Fanning	v33	*Porites*	-159,35	3,85	6605±13	1	24	1	0	Cobb et al. (2013)
Fanning	v11	*Porites*	-159,35	3,85	6897±15	1	37	1	0	Cobb et al. (2013)
Chritsmas	xmas_mod_spl	*Porites*	-157,40	1,87	12±0	1	69	1	0	Cobb et al. (2013)
Chritsmas	m2	*Porites*	-157,40	1,87	434±8	1	46	1	0	Cobb et al. (2013)
Chritsmas	p49	*Porites*	-157,40	1,87	1267±5	1	19	1	0	Cobb et al. (2013)
Chritsmas	p2	*Porites*	-157,40	1,87	1705±5	1	21	1	0	Cobb et al. (2013)
Chritsmas	p11	*Porites*	-157,40	1,87	2221±10	1	22	1	0	Cobb et al. (2013)
Chritsmas	p37	*Porites*	-157,40	1,87	2299±15	1	26	1	0	Cobb et al. (2013)
Chritsmas	p26	*Porites*	-157,40	1,87	3476±16	1	43	1	0	Cobb et al. (2013)
Chritsmas	p43	*Porites*	-157,40	1,87	3841±17	1	43	1	0	Cobb et al. (2013)
Chritsmas	p40	*Porites*	-157,40	1,87	3974±18	1	48	1	0	Cobb et al. (2013)
Chritsmas	p34	*Porites*	-157,40	1,87	4110±13	1	69	1	0	Cobb et al. (2013)
Chritsmas	p382	*Porites*	-157,40	1,87	4977±14	1	37	1	0	Cobb et al. (2013)
Chritsmas	p381	*Porites*	-157,40	1,87	5019±16	1	27	1	0	Cobb et al. (2013)
Christmas	XM35	*Porites*	-157,40	1,87	4373±10	1	176	1	0	McGregor H. et al. (2013)
EP										
South Peru	ICA+Llostay	*Mesodesma*	-75,57	-14,87	-28,5±18	1	34	1	0	Carré et al. (2014)
South Peru	Chala	*Mesodesma*	-74,21	-15,77	486,5±41	1	21	1	0	Carré et al. (2014)
South Peru	ICA-IS2	*Mesodesma*	-75,56	-14,87	457,5±72	1	26	1	0	Carré et al. (2014)
South Peru	Lomas	*Mesodesma*	-74,85	-15,57	582,5±67	1	20	1	0	Carré et al. (2014)
South Peru	Asia 3+5	*Mesodesma*	-76,60	-12,77	2906±121	1	19	1	0	Carré et al. (2014)
South Peru	Ancon	*Mesodesma*	-77,18	-11,78	3074±116	1	15	1	0	Carré et al. (2014)
South Peru	QLB-H4	*Mesodesma*	-70,83	-18,02	4663±136	1	14	1	0	Carré et al. (2014)
South Peru	ICA-IN	*Mesodesma*	-75,57	-14,87	6775,5±121	1	17	1	0	Carré et al. (2014)
South Peru	QLB-N2+N3	*Mesodesma*	-70,83	-18,02	7142±405	1	15	1	0	Carré et al. (2014)
South Peru	QLB-N4	*Mesodesma*	-70,83	-18,02	8500±451	1	10	1	0	Carré et al. (2014)
South Peru	QLB-N5	*Mesodesma*	-70,83	-18,02	9129±123	1	13	1	0	Carré et al. (2014)
South Peru	QLB-N6	*Mesodesma*	-70,83	-18,02	9369±65	1	13	1	0	Carré et al. (2014)
South Peru	QLB-N7	*Mesodesma*	-70,83	-18,02	9461±154	1	34	1	0	Carré et al. (2014)

throughout the transient simulation. The transient simulation starts from the last year of a mid-Holocene simulation that was run following the PMIP4 mid-Holocene orbital and trace gas changes (Otto-Bliesner et al., 2017). Results from this simulation have been discussed in Braconnot et al. (2019a).

2.2.2. Description of the IPSL-CM6 simulation

The IPSL-CM6 simulation, was run with a version of the IPSLCM5A-MR model (Dufresne et al., 2013) in which the land surface component has been substantially modified to include a 11 layer hydrology, a new snow model and dynamical vegetation (Braconnot et al., 2019b). It can be seen as an intermediate version of the land surface ORCHIDEE model (Krinner et al., 2005) compared to the one implemented in IPSLCM5 (Dufresne et al., 2013) and IPSLCM6 (Boucher et al., 2020). A detailed model description and assessment of model performance is given in Braconnot et al. (2019b) and results from this simulation have been discussed in Braconnot et al. (2019a).

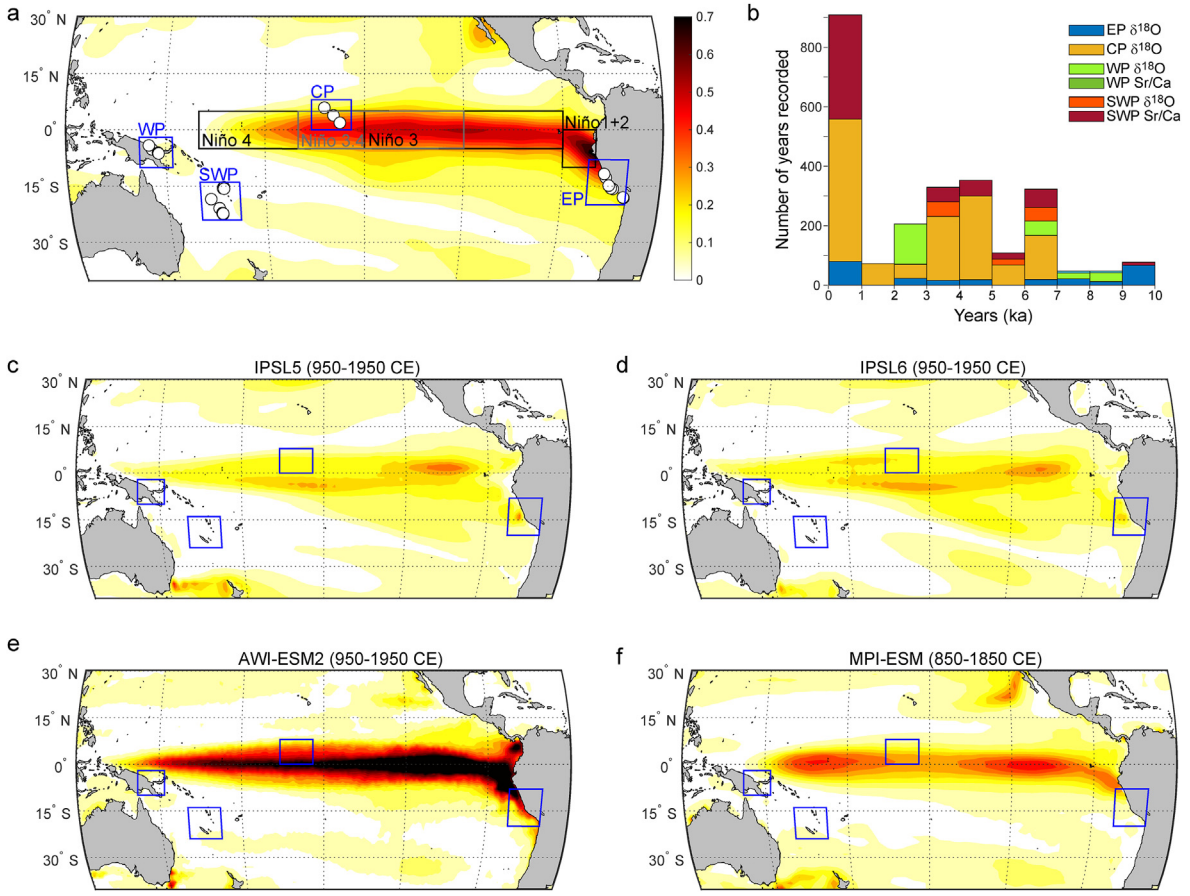

Fig. 1. (a) Map of archive location. Color shades indicate the variance of the sea surface temperature interannual variability (2–7 year band-pass filter) using NOAA ERSST(v5) monthly SST data from 1900 to 2017 (Huang et al., 2017). The EP, CP, WP and SWP regions defined for coral and mollusk archive groups are shown in blue, while Niño1+2, Niño3 and Niño4 boxes are shown in black and Niño3.4 in grey. (b) Cumulated number of years recorded per millenia, separated by region and by proxy type ($\delta^{18}O$ or Sr/Ca). (c–f) Maps of the variance of the sea surface temperature interannual variability (2–7 year band-pass filter) in IPSL-CM5, IPSL-CM6, AWI-ESM2, and MPI-ESM models in preindustrial conditions (here the last 1000 years of the transient simulations). Same legend as for (a). (For interpretation of the references to colour in this figure legend, the reader is referred to the Web version of this article.)

Table 2
Main characteristics of paleoclimate transient simulations.

	IPSL-CM5	IPSL-CM6	AWI-ESM2	MPI-ESM
Atmosphere grid (lat, lon)	1.875 ° × 3.75 °	1.25 ° × 2.5 °	1.875 ° × 1.875 °	1.875 ° × 1.875 °
Atmosphere vertical levels	39	39	47	47
Ocean grid	2° (refined in the equatorial belt)	2° (refined in the equatorial belt)	1° (global ocean) ~0.22° (Arctic) ~0.33° (Equatorial belt)	1.5°
Ocean vertical levels	31	31	48	40
Carbon cycle	interactive	interactive	interactive	interactive
Vegetation	prescribed	dynamic	dynamic	dynamic
Time period (years BP[a])	6000–0	6000–0	6000–0	7950–100
Orbital forcing	Berger (1978)	Berger (1978)	Berger (1978)	Berger (1978)
Greenhouse gases	Otto-Bliesner et al. (2017)	Otto-Bliesner et al. (2017)	Ice cores Köhler et al. (2017)	Ice cores (see Dallmeyer et al., 2020)

[a] BP = before A.D. 1950.

2.2.3. Description of the AWI-ESM2 simulation

AWI-ESM2 is an extension of the AWI climate model version 2 (AWI-CM2) (Sidorenko et al., 2019) for earth system modeling (https://fesom.de/models/awi-esm/). The atmospheric module is represented by the general circulation model ECHAM6 (Stevens et al., 2013) (here in T63 horizontal resolution, ~180 km) including a land surface model (JSBACH) which is based on a tiling of the land surface and includes dynamic vegetation with 12 plant functional types and two types of bare surface (Reick et al., 2013). The ocean model is based on FESOM2 (Danilov et al., 2017). This model has been used in a number of applications (e.g., Lohmann et al., 2020; Vorrath et al., 2020; Kageyama et al., 2021). The current version of FESOM2 is available from the public GitHub repository at https://github.com/FESOM/fesom2 under the GNU General Public License (GPLv2.0).

2.2.4. Description of the MPI-ESM simulation

The MPI-ESM includes the atmospheric model ECHAM6

(Stevens et al., 2013). The ocean module is MPI-OM (Jungclaus et al., 2013), which includes a sea-ice model and the biogeochemical chemistry model HAMOCC (Ilyina et al., 2013). The land-surface module, JSBACH (Reick et al., 2013) includes dynamic vegetation. The model version applied here includes several updates and corrections compared to the CMIP5 version (Giorgetta et al., 2013) and is identical to the model used in the MPI "Grand Ensemble" project (Maher et al., 2019). The Holocene transient simulation corresponds to the simulation with dynamical vegetation presented in Dallmeyer et al. (2020). Greenhouse gas concentrations were taken from an updated version of the one used in Schmitt et al. (2012) (Dallmeyer et al., 2020). The transient simulation was begun after a 3000 year spin-up, with constant boundary conditions fixed at 7950 BP (Dallmeyer et al., 2020).

3. Methods

3.1. Estimating seasonality and interannual variability changes

The seasonality and interannual variability were calculated for each individual record. Seasonality was here defined as the average amplitude of the annual cycle (maximum monthly SST - minimum monthly SST in a calendar year). The interannual variability for corals and long-lived bivalves (>10 years) was calculated as the variance of the annual means after filtering out low frequency variability (>10 years). For short-lived (typically 1–5 years) bivalves from Peru, the interannual variability was estimated as the variance of the seasonal amplitudes obtained from a group of shells collected in the same depositional unit (i.e. the same period), which has been shown to be a good measure of the interannual variability of the Niño1+2 index (Carré et al., 2005a, 2013, 2014).

Anomalies in interannual variability were estimated as relative deviations from the modern reference record from the same taxon collected in the same locality (equation (1)):

$$Va = \frac{V(\text{fossil}) - V(\text{modern})}{V(\text{modern})} \quad (1)$$

where V is the interannual variability and Va the interannual variability anomaly. Anomalies of seasonality were calculated in a similar way. The modern reference records all date to after 1900 CE. One 350 year-long modern record was divided into a modern reference (post 1900 CE) and a fossil record (pre 1900 CE).

We used relative deviations following Emile-Geay et al. (2016) because: (1) the values obtained are unitless, allowing comparisons between results from Sr/Ca and $\delta^{18}O$ records, (2) the anomaly is independent of any empirical calibration and is therefore not affected by calibration uncertainty, (3) biases specific to species and local conditions are minimized, (4) the amplification of variance changes in aragonite $\delta^{18}O$ records due to the influence of water $\delta^{18}O$ variability (Russon et al., 2013; Thompson et al., 2011) is reduced (though not cancelled) because the linear term in the relationship between SST and salinity is eliminated.

Seasonality and interannual variability in simulations were calculated using monthly values as in the coral and bivalve records. The last 1000 simulated years from each simulation were used as a modern reference to evaluate relative changes in the past. We did not correct for paleo-calendar changes. However, since the seasonality is here calculated as the total annual range, both for observations and models, changes in the phase of extrema do not affect our results. While tropical SSTs are not significantly affected by the paleo-calendar, there is still a non-negligible impact on the annual range of precipitation, especially in the western tropical Pacific (Bartlein and Shafer, 2019), but it is assumed that the impact is likely to be smaller than the uncertainties in the observations over the timeframe considered.

3.2. Estimating uncertainties

Holocene paleo-ENSO records are expected to provide an estimate of ENSO statistics at the millennial timescale. However, most records cover shorter windows (42 years in average) of time and therefore represent particular periods within a millennium. Long periods with high or low ENSO variability can occur without external forcing (Wittenberg, 2009), so we need to account for the possibility that the reconstructions could be biased towards a period with high or low variability rather than being representative of millennial scale conditions. This sampling of the stochastic modulation of ENSO is the main source of uncertainty when reconstructing millennial scale ENSO changes from short coral and bivalve records. It depends primarily on the amplitude of the variability in the study site and on the length of the record (Carré et al., 2012a). Estimating this uncertainty is required to detect forced changes.

We estimated the uncertainty of the seasonality and interannual variability for each record using a Monte Carlo sampling approach (Carré et al., 2012a). A window the same length as the record was randomly drawn from a time series of SSTs representative of the study site. Stochastic noise representing the analytic uncertainty and the monthly water $\delta^{18}O$ variability was then added to each datapoint (white gaussian noise, $\sigma = 0.4$ °C, bounded in ±0.8 °C). Then the seasonality and the interannual variability of this sample were calculated and compared to the actual values of the whole time series. The standard deviation obtained from 10,000 sampling iterations yields a standard error for each record for the estimation of the statistics of the whole period. This standard error primarily depends on the length of the record, and the amplitude of the variability (Carré et al., 2012a).

Uncertainties for modern reference records were calculated using instrumental SSTs from the NOAA ERSST.v5 monthly dataset (Huang et al., 2017). For each record, the 1900–2017 instrumental SST time series was calculated as the average of the nine grid points around the site location.

The instrumental record is too short to estimate the uncertainties for fossil records, which sometimes exceed 100 years in length. We therefore used monthly SSTs from the last 1000 years of a transient simulation averaged over the region in which the record was located. We arbitrarily used the IPSL-CM5 simulation for this, but since the amplitude of multidecadal to centennial modulation of ENSO is similar across models (see result section 4.2), this choice is unlikely to have affected the estimate. The effect of model biases is minimized because we use relative anomalies. The effect of sampling the centennial unforced variability is therefore included in the uncertainty value, even though the centennial scale modulation of ENSO may be under- or over-estimated by the model. This approach is consistent with climate dynamics and provides an indication of the significance of the change measured in the fossil record (Russon et al., 2015).

The uncertainty of the interannual variability anomaly was propagated using equation (2), which assumes that anomalies in fossil records are independent from modern anomalies:

$$\sigma_a = (Va + 1) \cdot \sqrt{\frac{\sigma(\text{fossil})^2}{V(\text{fossil})^2} + \frac{\sigma(\text{modern})^2}{V(\text{modern})^2}} \quad (2)$$

Where σ_a is the uncertainty of the interannual variability anomaly, σ the uncertainty of the record's seasonality, V is the interannual variability and Va the interannual variability anomaly. Uncertainty was propagated in the same way for seasonality.

3.3. Building composite records

We reconstruct seasonality and interannual variability in the regions where there are records (EP, CP, WP, and SWP, as defined in section 2.1), rather than in the classic El Niño boxes, in order to reduce the risk of bias due to non-stationarity in the relationship between signals from different geographic regions. We then make a direct comparison between the composites for each region and the simulation for that region. The combined record in each region is calculated as the weighted mean of variance anomalies in a 1000-yr running window, similar to the approach of McGregor S. et al. (2013). Weights correspond to the length of the records in years. The uncertainty of the weighted mean is propagated using equation (3):

$$\sigma_m = \frac{1}{\sum_{i=1}^{n} N_i} \cdot \sqrt{\sum_{i=1}^{n} (Sa_i \cdot N_i)^2} \quad (3)$$

Where σ_m is the uncertainty of the seasonality weighted mean over the 1000-yr window, n the number of records in the 1000-yr window, Sa_i the seasonality anomaly of record number i and N_i the number of recorded years. We used an equivalent equation for the error propagation of interannual variance anomaly weighted mean.

The simulated interannual variability and seasonality were calculated in the same way as for coral records. The interannual variability was calculated as the variance of annual values in moving windows (1000, 100, and 25 years) after filtering out low frequencies (>10 years). The seasonality was calculated as the average annual range (maximum monthly value - minimum monthly value in a year) over the moving window. Changes were estimated as relative anomalies, in the same way as for the observations except that the modern reference period was the last 1000 years of the simulation. Using this long modern reference period minimizes the scatter related to centennial scale internal variability and thus makes anomalies more comparable between simulations.

3.4. Pseudo-carbonate $\delta^{18}O$ from climate simulations

To evaluate biases in coral or bivalve $\delta^{18}O$ due to the mixed influence of temperature and water $\delta^{18}O$, the records were compared to both simulated SSTs and to pseudo-aragonite $\delta^{18}O$ modelled from climate model outputs as a linear combination of SST and sea surface salinity (SSS) (Brown et al., 2008a, 2008b; Thompson et al., 2011) as follows:

$$\delta^{18}O_{\text{pseudo-aragonite}} = a_1 \cdot T + a_2 \cdot S \quad (4)$$

Where T is sea surface temperature, S is sea surface salinity, a_1 and a_2 are constant coefficients. Coefficient a_1 corresponds to the temperature dependence of oxygen fractionation in biogenic aragonite. Published estimates for corals and bivalves range from −0.17 to −0.23‰/°C (Evans et al., 2000; Gagan et al., 2012; Grossman and Ku, 1986; Juillet-Leclerc and Schmidt, 2001; Lough, 2004); we used an intermediate value of a_1 = −0.21‰/°C. Coefficient a_2 represents the slope of the relationship between sea water $\delta^{18}O$ and salinity. We used the mean value of a_2 = 0.27‰/psu estimated for the tropical Pacific (Fairbanks et al., 1992; LeGrande and Schmidt, 2006). The forward model does not take account of the spatial and temporal variability of the $\delta^{18}O$-SSS relationship seen today in the tropical Pacific (Conroy et al, 2014, 2017, 2014; Stevenson et al., 2013), and in isotope-enabled models (LeGrande and Schmidt, 2011; Stevenson et al., 2018). Values of a in the eastern and central Pacific tend to be lower than those from the western and southern Pacific (Russon et al., 2013; Stevenson et al., 2018). Estimating changes as anomalies minimizes the site-specific variability of the $\delta^{18}O$-SSS relationship but does not correct for the temporal variability in the $\delta^{18}O$-SSS relationship.

3.5. Sampling strategy for model-data comparison

Model-data comparisons are performed using ENSO and seasonality statistics over 1000-yr windows. The sampling of unforced modulation of ENSO by short records within the 1000-yr window must be accounted for also in the model-data comparison. We do this in two ways. First, we computed the distribution of simulated variability over 100-yr and 25-yr windows for the successive 1000-yr intervals, so as to evaluate the scatter related to internal variability at time scales comparable to the length of the coral and bivalve records. Second, we constructed the probability density function (pdf) of seasonality and interannual variability anomalies for each millennium and region by sampling the simulated time series randomly 10,000 times for windows whose number and size was determined by the records available in the same region and millennium. Pdfs were constructed separately for the SST and the pseudo-aragonite $\delta^{18}O$ time series. Millennial trends reconstructed from the records were compared to the simulation ensemble. The trajectories of interannual variability and seasonality obtained from the SSTs and pseudo-$\delta^{18}O$ provide an ensemble of 8 members for each region and the ensemble trend was the median of these 8 members. The internal centennial variability was represented as the density of values obtained from 100-yr windows within running 1000-yr windows, with confidence intervals represented by the 0.05 and 0.95 quantiles.

3.6. Estimating Eastern Pacific and Central Pacific modes

We use a simplified approach to estimate the changes between the East Pacific (E) and Central Pacific (C) modes that can be computed from both the variability reconstructions from paleoclimate archives and model results. Our objective is to investigate if we can isolate a long-term tendency in the westward and southeastward ENSO variability by comparing the changes in variance with time in the EP and CP regions where the paleoclimate reconstructions are available. We define $R_{E/C}$ as the ratio of interannual variability in the two regions, to evaluate past changes in ENSO spatial modes independently from changes in overall intensity as follows:

$$R_{E/C} = \frac{V_{EP}}{V_{CP}} \quad (5)$$

Where V_{EP} and V_{CP} are the interannual variability of SST in the EP and CP regions. The associated uncertainty σ_R is propagated as follows:

$$\sigma_R = R_{E/C} \cdot \sqrt{\frac{\sigma_m(V_{EP})^2}{V_{EP}^2} + \frac{\sigma_m(V_{CP})^2}{V_{CP}^2}} \quad (6)$$

We tested if our approximation provides a reliable estimate of the relative contribution of E and C modes using the NOAA ERSST.v5 instrumental SST time series over the period 1900–2017. Changes in the interannual variability were estimated by the 10-yr running variance of annual values and normalized by the variance over the whole period. Takahashi et al. (2011) define ENSO flavours by the E and C indices (modes defined by a 45° rotation of the first two principal components of tropical Pacific SST). They further show that it can be approximated by E ≈ $Niño_{1+2}$−0.5 $Niño_4$, and C ≈ 0.7 $Niño_4$ − 0.1 $Niño_{1+2}$ (Takahashi et al., 2011). We find that the

interannual variability of SSTs in the EP and CP regions provides a good approximation of E and C modes (Fig. 2) even though this diagnosis does not isolate ENSO flavours as defined by (Takahashi et al., 2011). The differences with the original estimates are larger for E, since our EP box is located further south than the Niño1+2 box in the original definition, and some E events that are maximal in the East Pacific might not have the same strength along the equator or further south. Small differences found for the C mode also reflect the difference between the variance recorded in the Niño4 regions and the different CP region used here.

3.7. Detection and attribution of insolation forcing

The statistical significance of the difference between ENSO variability during the Holocene ENSO minimum (HEM) period and the late Holocene was tested using a randomized permutation test in Matlab™ (function permutationTest, Krol, 2020) with 10,000 permutations. The test was applied to records from CP, from EP, and to transient simulations using interannual variability values in 100-yr windows.

The attribution test is here based on the significance of the relationship between the recorded values of ENSO variance and those obtained in insolation-forced simulations at the same time (Hegerl and Zwiers, 2011; Stott et al., 2010). We considered only the 6–0 ka period, common to the four simulation, when the polar ice sheets have reached their modern size. The scaling factor (Hegerl and Zwiers, 2011; Stott et al., 2010) between simulated and reconstructed ENSO variance, defined by equation (7), was estimated as the slope of errors-in-variable linear regression, here a total least square linear regression computed as the slope of the first principal component.

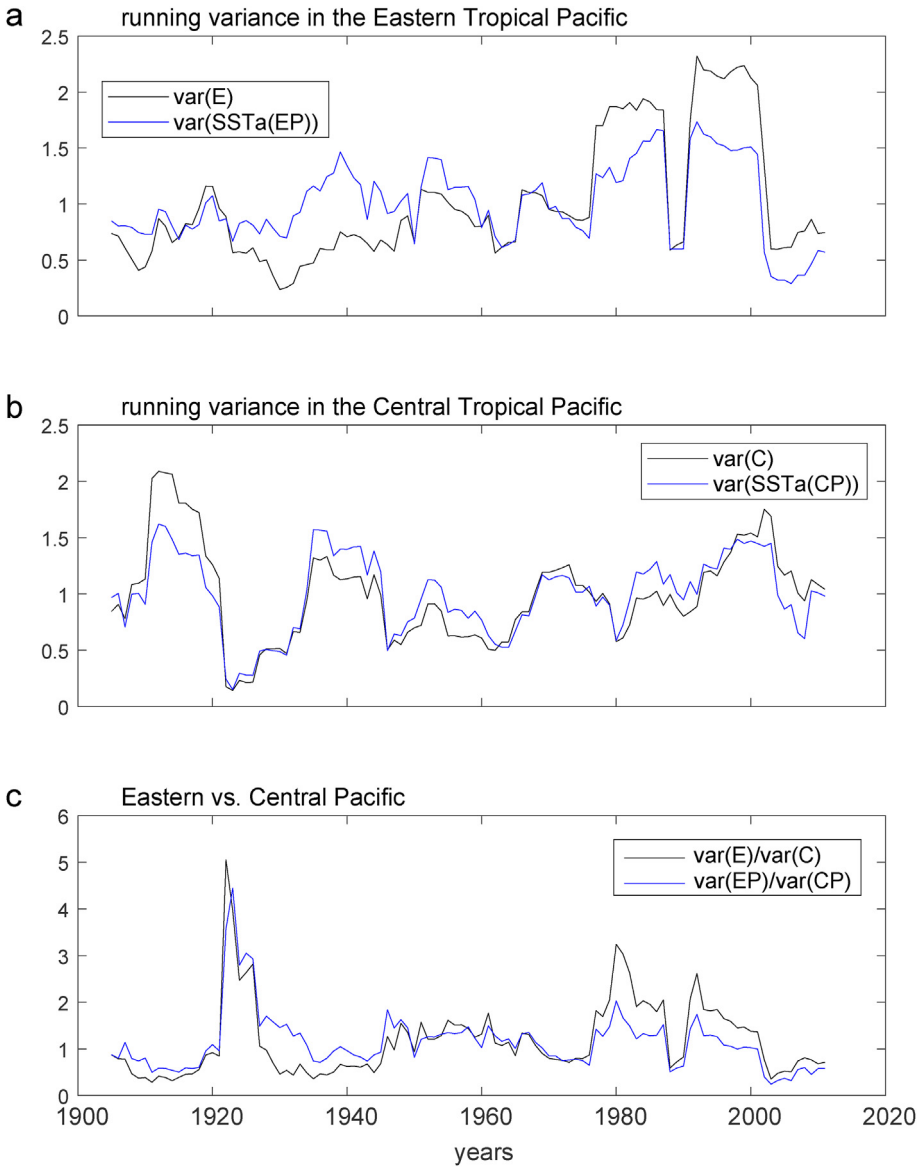

Fig. 2. (a) Interannual variability of E index compared to the interannual variability of SST in the EP regions (Fig. 1). (b) Interannual variability of C index compared to the interannual variability of SST in the CP regions. NOAA ErSSTv5 instrumental monthly SST from 1900 to 2017 were used (Huang et al., 2017). E and C indices were approximated from Niño1+2 and Niño4 SST (Takahashi et al., 2011). Monthly SST anomalies were calculated in reference to the whole period. The interannual variability is calculated as the variance of SST anomalies over 10-yr moving windows. (c) Comparison of the Eastern/Central Pacific ratios of variance using E and C indices (black) and SSTa from EP and CP regions (blue). (For interpretation of the references to colour in this figure legend, the reader is referred to the Web version of this article.)

$$V_{record} = \alpha \cdot V_{simulation} + u_0 \quad (7)$$

Where V_{record} is ENSO interannual variability measured in individual coral records, $V_{simulation}$ is ENSO interannual variability estimated in the 1000-yr windows centered on records ages, α is the scaling factor, and u_0 is the regression residual which represents the internally generated variability. The confidence interval of α was estimated at the 0.05 confidence level by a bootstrap procedure with 10,000 iterations (DelSole et al., 2019). Scaling factors were estimated for the CP region only using both SST and pseudo-aragonite $\delta^{18}O$ in the four simulations, and in the ensemble combining SST and pseudo-aragonite $\delta^{18}O$. Attribution to external forcing is validated if the scaling factor α is significantly greater than 0. The effects of greenhouse gases and orbital forcing are not formally separated.

4. Results

4.1. Data-inferred changes in interannual variability and seasonality during the holocene

4.1.1. Interannual variability

Interannual variability is reduced in the WP, CP and EP during of the whole Holocene compared to the post-1900 CE interval, indicating that ENSO activity is anomalously high in the 20th century (Fig. 3). The trends in interannual variability in EP and CP are coherent to first order. A statistically significant minimum variability occurs between 3 to 6ka; interannual variability before 6ka is not significantly different from that in the late Holocene. The timing of the HEM is poorly constrained because of the sparsity of data but may have lasted 2000–3000 years. All the records point to stronger ENSO activity after 3ka compared to 4-6ka, but the transition is only recorded in the CP, where it appears gradual. In the WP, the interannual variability is similar to modern by 2ka, but strongly reduced before that. The variability in WP in the early Holocene is lower compared to the EP and CP. There are no records from this region between 6 and 4ka, so it is not possible to detect the minimum seen in the EP and CP regions at that time. The maximum reduction in interannual variability is *ca.* 80 % in the WP and CP regions but only ca 50 % in the EP region.

The reconstructed changes in the SWP are different. Interannual variability is generally larger during the Holocene than the modern reference period (Fig. 3). The maximum increase (200 %) occurs between 6 and 4 ka, coincident with the minimum variability in the CP and EP regions. These large anomalies are partly due to the low modern variability. The increased variability is reasonably robust since it is recorded by 3 different corals. Increased variability in the mid-Holocene is apparent in both $\delta^{18}O$ and Sr/Ca records, although the increase is generally larger in Sr/Ca records.

There are large fluctuations in the var(EP)/var(CP) ratio in the early Holocene, and a slightly decreasing trend after 4.5ka (Fig. 4) (trends are forward through time). However, the variations in the reconstructed var(EP)/var(CP) ratio are not statistically significant due to the large uncertainties.

4.1.2. Seasonality

The patterns of change in seasonality through time (Fig. 3) are highly variable. Seasonality in the EP is similar or less than present. Intervals of significantly lower interannual variability tend to be intervals with reduced seasonality (e.g. between 4-6ka) but the early Holocene is characterised by only a small reduction in interannual variability and a large reduction in seasonality. CP and WP records show both reduced and increased seasonality, with changes between −30 % and +30 % compared to the recent interval. The intervals of reduced seasonality are intervals when inter-annual variability is highly reduced, whereas intervals of enhanced seasonality generally correspond to intervals when the reduction in interannual variability is less. The SWP records also show both reduced and increased seasonality (−10 and + 50 %). However, there appears to be no coherence between the change in seasonality and the change in interannual variability. The temporal congruence between changes in seasonality and interannual variability seen in some regions and time periods must be a function of dynamical linkages, since the reconstructions of these two variables are mathematically independent. Comparison of records from the WP and SWP shows that the $\delta^{18}O$ records have lower seasonality anomalies than Sr/Ca records in the early Holocene, suggesting the overall change in seasonality reflects change in rainfall seasonality.

The change in seasonality does not directly follow the insolation seasonal contrast which is characterised by a decreasing trend through the Holocene in the northern hemisphere and an increasing trend in the southern hemisphere. Lazareth et al. (2013) already pointed out that the changes in seasonality in the SWP were opposite to what might be expected from the insolation forcing. This points to the importance of regional factors in affecting changes in seasonality. In the East Pacific, for example, climate simulations suggest that the upwelling was damped due to insolation forcing and surface winds (Braconnot et al., 2007; Luan et al., 2015).

4.2. Interannual variability and seasonality in transient simulations

Internal variability of ENSO (here defined as unforced changes of ENSO interannual variability) in models are shown in Fig. 5 on multidecadal time scale (shade), centennial time scale (dotted lines) and millennial time scale (continuous lines). The simulations consistently show increasing trends of interannual variability from the mid-Holocene to the present in the central equatorial Pacific (Niño3.4 and the CP region) with a 20–40 % reduction in ENSO variability in the mid-Holocene (Fig. 5). None of the simulations produced a smooth multimillennial trend in ENSO variability, showing that ENSO involves unforced internal variability at the millennial scale as well. Three of the models show an increasing trend in ENSO variability in the EP (Fig. 5e, f, h), but the simulated changes are not significantly different from the internal millennial variability in the AWI model (Fig. 5g). Interannual variability in the SWP does not increase significantly through the Holocene in any of the simulations (Fig. 5q, r, s, t). Models diverge in their response in the WP region: IPSL-CM5 has an increase in both SST and pseudo-aragonite $\delta^{18}O$ (Fig. 5m), IPSL-CM6 shows no trend in either (Fig. 5n), AWI has a decreasing trend in SST but an increasing trend in pseudo-aragonite $\delta^{18}O$ (Fig. 5o), while MPI shows no systematic trend in SSTs but an increasing trend in pseudo-aragonite $\delta^{18}O$ (Fig. 5p). Model behaviour in the WP is clearly affected by the representation of the warm pool and associated atmospheric convection. The amplitude of the unforced multidecadal and centennial variability, as shown by the 25-yr and 100-yr running windows, is ~±30 % around the millennial trend (Fig. 5). This amplitude (shaded area in Fig. 5) is similar in all models and all regions, for both SST and $\delta^{18}O$. There is no substantial change in this higher frequency variability except for SST in the AWI model in the WP region, where the multidecadal variability of ENSO is larger in the mid-Holocene (~±50 %) and decreases progressively thereafter (Fig. 5o). These results show that the amplitude of the decadal to centennial variability of ENSO variance in models is similar and often larger than the orbitally-forced trend, so that in any time, models can produce a short period of ENSO variability higher than at PI.

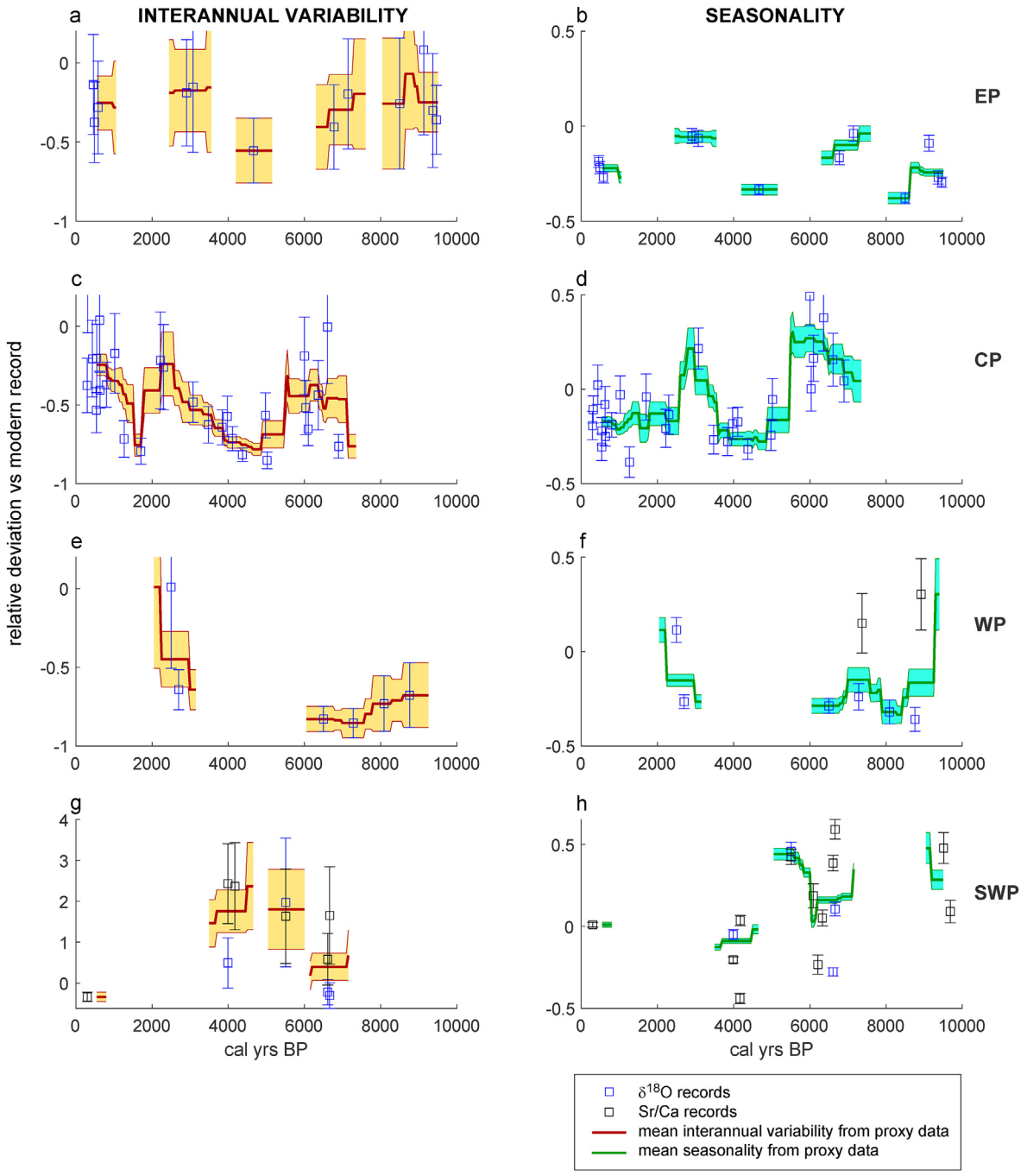

Fig. 3. Interannual variability and seasonality changes in archive records through the Holocene. Records are grouped by region: EP (a, b), CP (c, d), WP (e, f) and SWP (g, h). Changes in interannual variability are shown in the first column (a, c, e, g), and seasonality in the second column (b, d, f, h). For each record, the change is expressed as a relative deviation from a modern archive (post A.D. 1900). Error bars (±1σ) were estimated with a Monte Carlo resampling experiment using pseudoproxy modelling (see methods). The running mean of variance anomaly is represented (thick red line for variability, thick green for seasonality) with the corresponding propagated uncertainty (±1σ) (shade). (For interpretation of the references to colour in this figure legend, the reader is referred to the Web version of this article.)

The changes in simulated seasonality are smaller than those in interannual variability. Simulated seasonality increases from the mid-Holocene to the present in the EP, WP and SWP regions (Fig. 6), following the Southern Hemisphere insolation trend. The mid-Holocene reduction is generally about 10 %, except in the WP region in the MPI simulation (Fig. 6p) where the reduction in pseudo-$\delta^{18}O$ seasonality exceeds 30 %. The changes in seasonality shown by SSTs and $\delta^{18}O$ are generally similar for all models in these three regions, with the exception of the WP region in the AWI and MPI simulations (Fig. 6o, p) where the SST seasonality is much less than that of the $\delta^{18}O$. The multidecadal and centennial variability in simulated seasonality is small (<±5 %) and generally smaller than the orbitally-driven changes.

The models produce divergent results for the equatorial central Pacific (CP and Niño3.4 regions). IPSL-CM5 has an increasing trend in seasonality in all boxes (Fig. 6a, i), IPSL-CM6 has a decrease in CP or no trend in Niño3.4 (Fig. 6b, j), AWI has a strong increase in Niño3.4 but no trend in CP (Fig. 6c, k), and MPI shows in Niño3.4

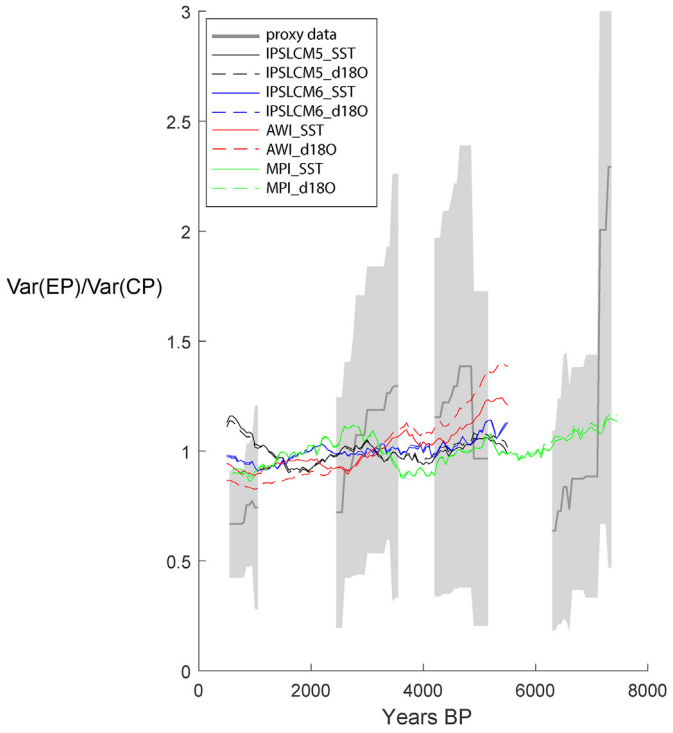

Fig. 4. Changes in the relative influence of ENSO over the Eastern Pacific vs the Central Pacific during the Holocene estimated by Var(EP)/Var(CP) ratios from archive records (grey), and in IPSL-CM5 (black), IPSL-CM6 (blue), AWI-ESM2 (red) and MPI-ESM (green) model simulations using SST (continuous lines) and pseudo-$\delta^{18}O$ (dotted lines). (For interpretation of the references to colour in this figure legend, the reader is referred to the Web version of this article.)

and CP a decrease through the early Holocene to a minimum around 4ka and a subsequent increase (Fig. 6d, l). The multidecadal to centennial variability in seasonality is larger (±5 to ±10 %) in the equatorial central Pacific than in the other regions in all of the models. Differences between models in this region are associate with the way the equatorial upwelling is represented and in particular its westward extension.

The trajectories of simulated var(EP)/var(CP) ratios show different results in the simulations. IPSLCM6 and AWI models show a decreasing trend of var(EP)/var(CP) ratios from the mid-Holocene to present using both SST or pseudo- $\delta^{18}O$ (Fig. 4). IPSLCM5 and MPI show millennial variability in the ratio but no consistent trend. The ensemble does not show a robust trend in the spatial pattern of ENSO linked to the imposed orbital insolation changes.

4.3. Model-data comparison, detection-attribution of insolation forcing

Interannual variability and seasonality in the model ensemble are compared to the combined records in Fig. 7 which provides a synthetic view. The pdf approach provides a way of accounting for the intrinsic irregularity of ENSO and the shortness of records in model-data comparisons (Fig. 8). In the WP, reconstructed interannual variability values in the 3rd millennium and between 6 and 8ka are below the simulated variability, even for the pseudo-$\delta^{18}O$ variability. However, reconstructed ENSO variance in the EP is within the range of the pdf derived from the simulations. Reconstructed values in the CP are at the lower end of or below the pdf curves from the simulations. The best agreement is found in the 3rd millennium, but the reconstructions are clearly below the simulations from 3 to 5 ka. Part of the discrepancy results from the anomalously high modern ENSO activity. Since the modern record reference is defined by the last 100 years or the last decades (depending on the locality), the larger modern variability could result from either anthropogenic greenhouse gases or from multidecadal to centennial internal variability or a combination of both. If the last millennium is used as a reference, the model ensemble is more comparable with the records in the CP region, although still above reconstructed ENSO variance 3 to 5 ka.

The variance of ENSO records in the HEM (here 3.1−5.9ka) is significantly lower compared to the Late Holocene (here 0.1−3.1ka) in the CP (randomized permutation test, $p = 0.003$, difference = 0.36). The recorded ENSO variance in the HEM in the EP is significantly lower than the modern variance but the difference is not statistically significant when compared to the late Holocene (randomized permutation test, $p = 0.143$, difference = 0.33). The variance of simulated ENSO is also significantly different between the HEM (3.1-6ka) and the Late Holocene (0.1−3.1ka) (randomized permutation test using 100-yr windows, 0.05 significance level) in both EP and CP regions in all simulations, using both SST or pseudo aragonite δ18O, with an average difference of 0.14 ± 0.07, about half the difference observed in records.

The scaling factor (equation (7)), is significantly positive for all the simulations except IPSL-CM5, and is also significantly positive for the multi-model median (Fig. 9), indicating that the increase of ENSO variance after 6ka is forced. The simulations are forced by changes in both insolation and greenhouse gases. However, since greenhouse gas forcing has little change over the Holocene, the simulated trend must reflect insolation forcing. The value of the scaling factor (4.7) means that ENSO sensitivity is much larger than indicated by the models. IPSL-CM5 model yields a very large error bar for the scaling factor, probably because of large internal millennial variability. The amplitude and to some extent the timing of the HEM are thus possibly a combination of insolation forcing and millennial scale internal variability.

5. Discussion

5.1. Timing of ENSO changes and insolation

Our synthesis expands on the previous study by Emile-Geay et al. (2016) by increasing the data coverage, including Sr/Ca records, and building composite records with quantified uncertainty in order to improve the robustness of the reconstructions, the ability to detect the effect of external forcing, and the objectivity of model-data comparisons. Nevertheless, our analysis confirms previous studies that identified a Holocene ENSO minimum (HEM) between 3-6ka in EP and CP using corals and bivalve data (Carré et al., 2014; Emile-Geay et al., 2016) and which was detected in the $\delta^{18}O$ variance of individual foraminifera in the EP (Koutavas and Joanides, 2012). Our uncertainty analyses show the HEM is significant compared to unforced multidecadal to centennial variability.

The timing of ENSO changes in the Holocene is an important clue to the relationship with insolation forcing. The HEM is in phase with part of the insolation forcing since it occurs during a maximum (minimum) of September−October insolation, and a minimum (maximum) of March−April insolation in the northern (southern) hemisphere. However, the dampening effect of insolation on ENSO is generally expected to be strongest 8-10ka, in the early Holocene, when the energy flux seasonal contrast was largest in the northern hemisphere (Braconnot et al., 2012b; Clement et al, 1999, 2000, 1999; Liu et al., 2014; Luan et al., 2012), a scenario that seems supported by some ENSO records related to the ITCZ (Conroy et al., 2008; Moy et al., 2002; Tudhope et al., 2001). Although a gradual increase is indicated by the Andean Lake Pallcacocha record (Moy et al., 2002; Rodbell et al., 1999) throughout the Holocene, the

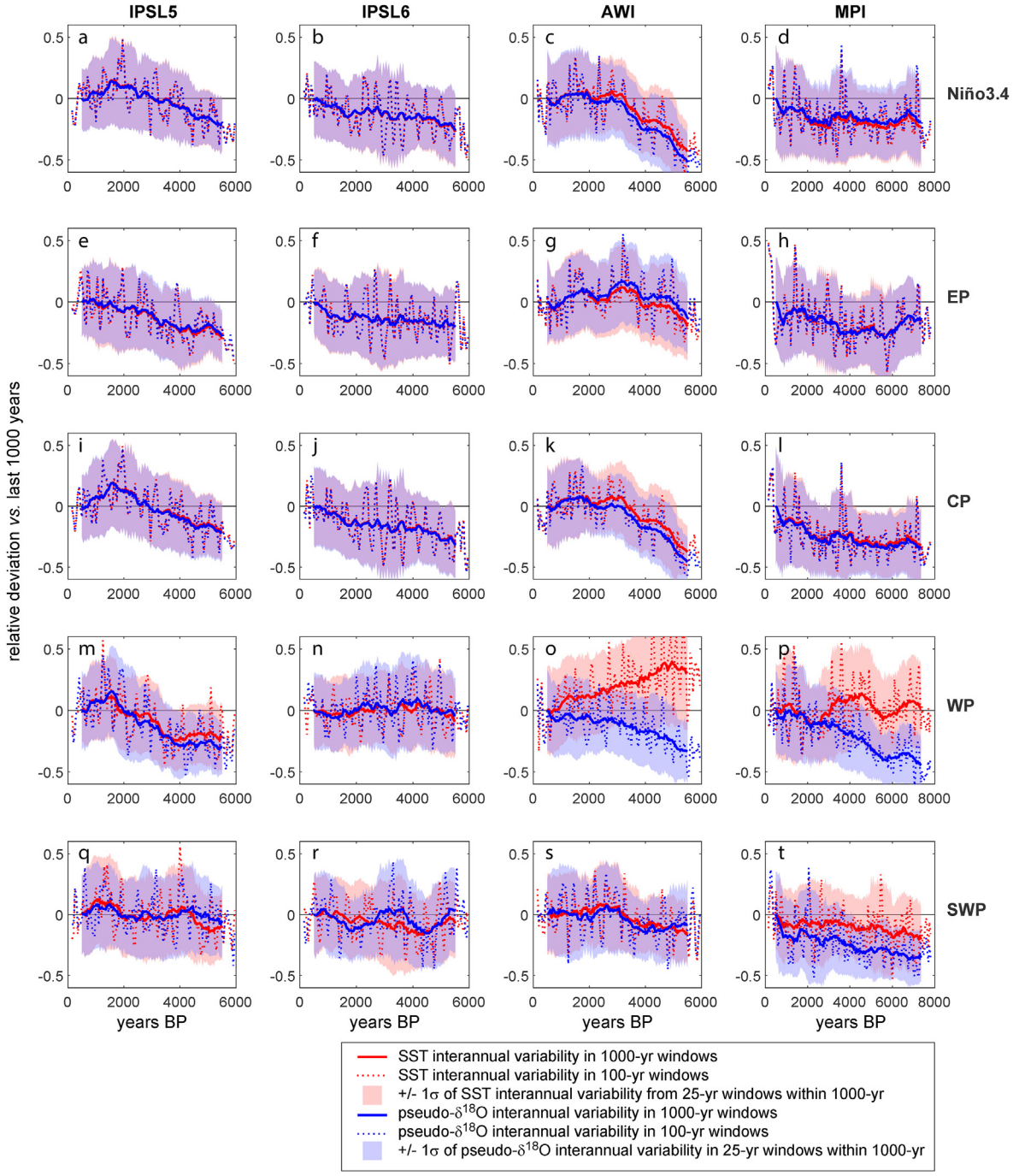

Fig. 5. Interannual variability changes in transient simulations. Interannual variability is calculated as a relative anomaly compared to the last 1000 years. The anomaly is calculated over running 1000-yr windows (thick lines) and 100-yr windows (dotted lines) for SST (red) and pseudo-aragonite $\delta^{18}O$ (blue). Shaded areas correspond to the standard deviation obtained from 25-yr windows within the 1000-yr windows. 25 year is a length typical of most coral records. Results are shown for IPSL-CM5, IPSL-CM6, AWI, and MPI climate models (columns 1 to 4) in the Niño3.4, EP, CP, WP, and SWP regions (lines 1 to 5), as defined in Fig. 1A. (For interpretation of the references to colour in this figure legend, the reader is referred to the Web version of this article.)

sensitivity of this region to El Niño events might have been reduced in the early Holocene (Kiefer and Karamperidou, 2019; Schneider et al., 2018) when the Eastern tropical Pacific was cooler (Carré et al., 2005b, 2012b; Koutavas et al., 2002), the ITCZ located further north (Haug et al., 2001; Sachs et al., 2018), the South American monsoon weaker and rainfall in Ecuador reduced (Mollier-Vogel et al., 2013). The interpretation of the Lake Junco record in the Galapagos for the early Holocene is also debated: while the sedimentological record has been interpreted as showing suppressed ENSO activity in the early Holocene (Conroy et al., 2008), variations in the concentration of green algae and their hydrogen isotopic ratio suggest ENSO activity was highly variable in the early Holocene and also pinpoints a minimum at 3-5ka (Zhang et al., 2014) in agreement with our records. Our results, in line with earlier simulations (Otto-Bliesner et al., 2003), suggest that the Holocene insolation-like signal in those rainfall-related ENSO records might be modulated by insolation-driven hydrological changes.

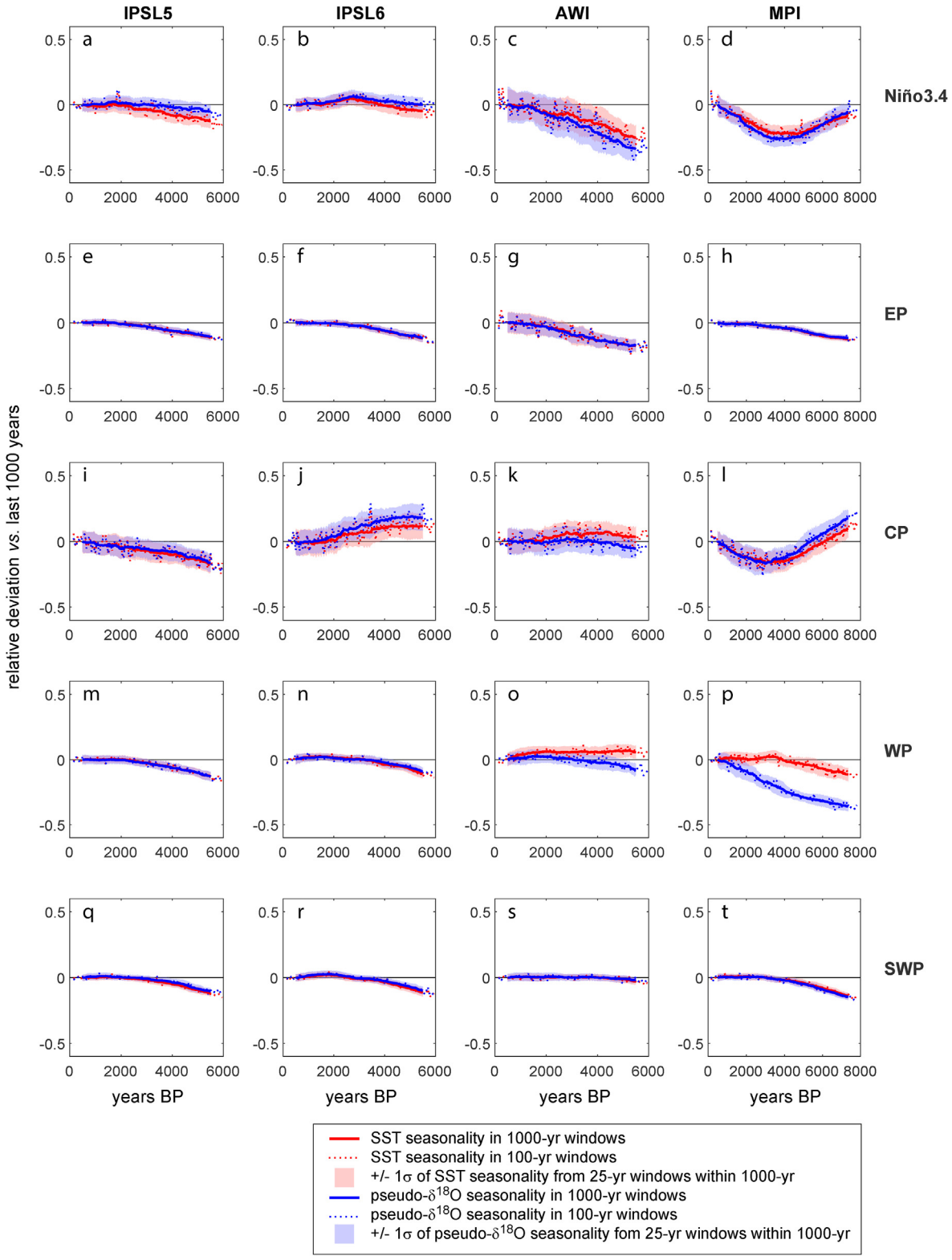

Fig. 6. Seasonality changes in transient simulations. Legend as in Fig. 5.

The large reduction of ENSO variability in the early Holocene in WP records compared to CP and EP records, may reflect either changes in ENSO flavours, different hydroclimate, or a combination of both. The simulations suggest that the impact of hydroclimate change on ENSO variance records in EP and CP is non-significant. However, two models show a divergence between the seasonality and ENSO activity estimated from SST and pseudo-$\delta^{18}O$ in the WP (and to a lesser extent in SWP) (Figure 5o, p), suggesting that hydroclimate changes may influence the $\delta^{18}O$ records in these regions. Since the short Sr/Ca records in WP indicate an increase of

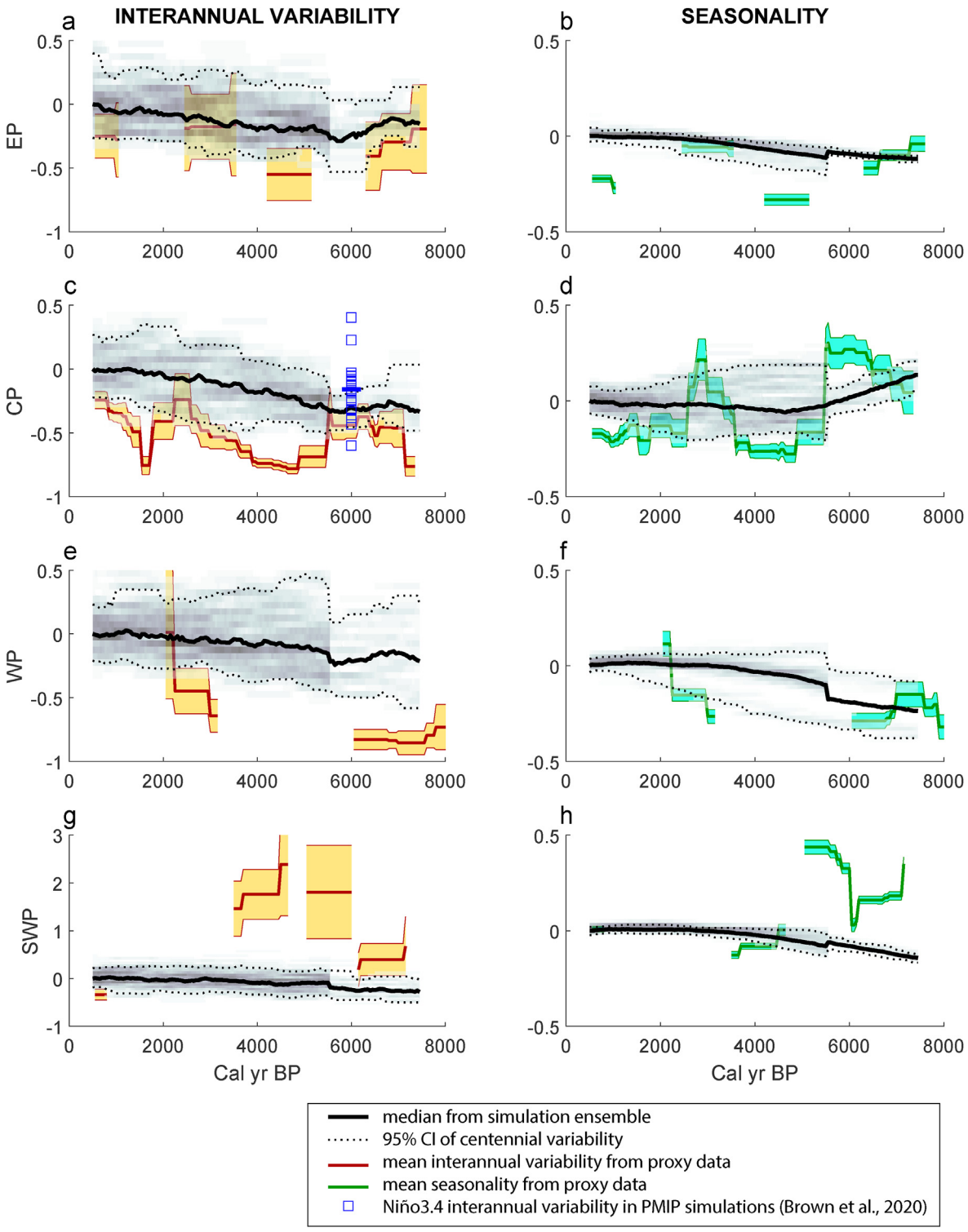

Fig. 7. Interannual variability and seasonality reconstructed trends compared to ensemble model trends. Reconstructions from proxies are represented as in Fig. 3. The simulation ensemble median (thick black line) includes trends from SST and pseudo- $\delta^{18}O$ in the four simulations represented in Figs. 5 and 6. The shading represents the distribution of values from 100-yr windows. The density of values is lower before 6ka because the 6-8ka period was only simulated by the MPI model. The 95 % confidence interval of the centennial variability is shown (dotted lines). Change in ENSO variance in mid-Holocene equilibrium simulations of CMIP5/PMIP3 and CMIP6/PMIP4 models calculated by Brown et al. (2020) are shown in the CP panel as blue squares. The ensemble mean is represented as a thick blue line. Note that the values were calculated for the Niño3.4 box, which is different from the CP box used in this study, and that change was calculated by reference to PI control simulations rather than the past 1000 years of the simulations as in this study. (For interpretation of the references to colour in this figure legend, the reader is referred to the Web version of this article.)

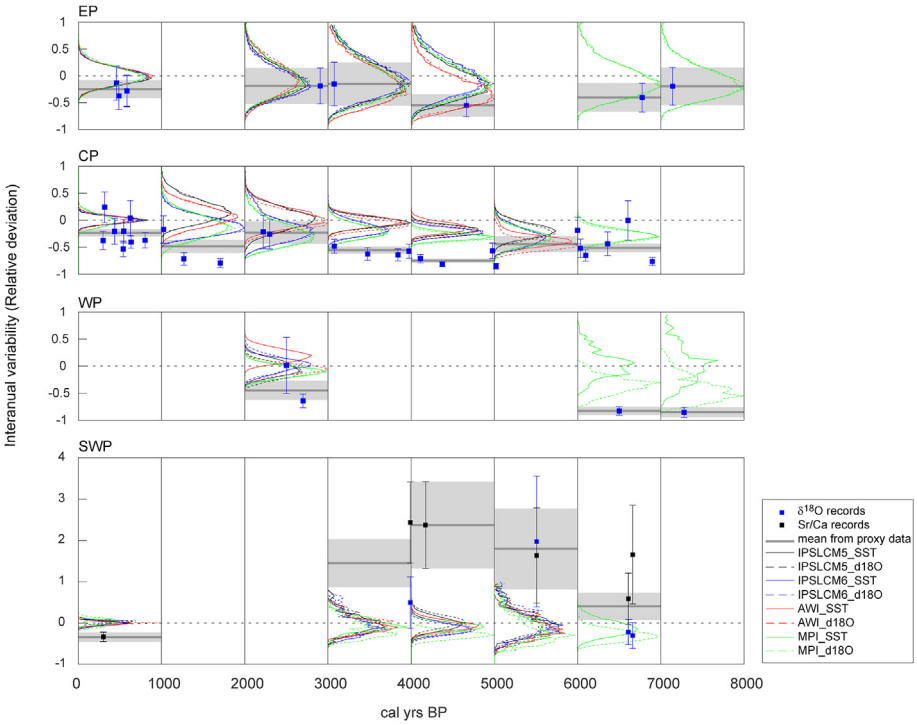

Fig. 8. Probability of obtaining the reconstructed values from the simulations. The pdf of mean interannual variability change derived from the random sampling of the simulations (see method section 3.7) are shown for IPSL-CM5 (black), IPSL-CM6 (blue), AWI-ESM2 (red) and MPI-ESM (green) models. Pdf curves of interannual variability anomalies are shown for SST (continuous lines) and pseudo aragonite $\delta^{18}O$ (dashed lines). Reconstructed interannual variability changes are represented per millennia and per region (grey thick lines). The values from individual $\delta^{18}O$ (black squares) and Sr/Ca (grey squares) records are also shown. (For interpretation of the references to colour in this figure legend, the reader is referred to the Web version of this article.)

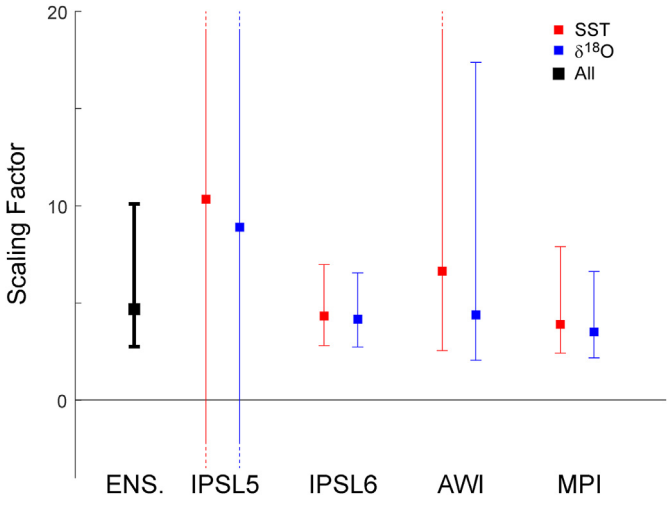

Fig. 9. Scaling factor between recorded and simulated ENSO variance in CP box 6-0ka, using simulated SST (red), pseudo d18O (blue), and for the simulation ensemble combining both SST and pseudo-d18O (black). Error bars represent the 95 % confidence interval (with dotted ends when larger than the graph scale). (For interpretation of the references to colour in this figure legend, the reader is referred to the Web version of this article.)

SST seasonality in the early Holocene which is opposite to the decrease obtained from $\delta^{18}O$ it is reasonable to suppose that the mid to early Holocene ENSO-related SST variability in the WP was not as reduced as implied by the coral and bivalves $\delta^{18}O$. A high-resolution speleothem isotopic record from Borneo shows lower interannual variability 3-6ka compared to the late Holocene and early Holocene (Chen et al., 2016) in agreement with the EP and CP records. Located 3800 km east of the WP box, in the core of the warm pool which showed no sign of cooling in the Holocene (Linsley et al., 2010), this new record from Borneo supports the hypothesis that the reduction of ENSO in WP coral and bivalves in the early Holocene might be overestimated.

The centering of the HEM ca. 4-5ka does not rule out insolation forcing of ENSO changes over the 6-0ka period used for model-data comparison. Our detection-attribution approach supports an insolation-driven increase of ENSO variance from 6ka to the present and an increasing trend of ENSO variance with insolation is a robust feature of the simulations. The relationship between insolation and ENSO variability is consistent with the fact that insolation is the main driver of climate changes during this period, because changes in GHG forcing in the later Holocene are very small. Changes in solar irradiance or volcanic forcing might influence ENSO variance. However, the fact that an increasing trend of ENSO variance with insolation is seen in MPI-ESM simulations when these additional forcings are included (Jungclaus, pers. comm.) suggests this is not the case. ENSO seems, however, much more sensitive in the real world than in models. The change in ENSO variability from 6ka to 0ka is 4.7 times larger in observations than in models. The low sensitivity of ENSO in models, also found in equilibrium mid-Holocene simulations (Brown et al., 2020) (Fig. 7), is not clearly understood and could be represents an issue for future predictionsprojections. However, the difference in reconstructed and simulated sensitivity may be overestimated, in part because the observed HEM could be affected by millennial scale internal unforced variability reinforcing the insolation signal and in part because our analysis is only based on CP records, and could also be affected by changes in the spatial pattern of ENSO.

The high ENSO variance before 6ka, however, is inconsistent

with the influence of insolation on ENSO dynamics and points to a role for other mechanisms. A number of other factors may be important for tropical variability during the early Holocene. The presence of vegetation in the Sahara, for example, due to the strengthening of the northern hemisphere monsoons and increased Mediterranean winter rainfall (Cheddadi et al., 2021) during the early Holocene resulted in a reduction of atmospheric dust loadings and modification of tropical teleconnections and ENSO (Pausata et al., 2017). At the same time, the melting of the remnant Laurentide ice sheet produced freshwater discharges to the North Atlantic and a rapid sea level rise (Bard et al., 1996). "Hosing" model experiments have showed that freshwater discharges in the North Atlantic tend to shift ENSO anomalies to the eastern Pacific and to increase its amplitude (Dong and Sutton, 2007; Timmermann et al., 2007; Williamson et al., 2018). Paleoclimate simulations also suggest that polar ice sheets and meltwater fluxes have a positive impact on ENSO interannual variability which may have offset the impact of insolation in the early Holocene (Braconnot et al., 2012b; Liu et al., 2014; Luan et al., 2015) and in the deglaciation (Liu et al., 2014). This hypothesis is also supported by reconstructions of high ENSO variance during the deglaciation (Sadekov et al., 2013). Our early Holocene records thus add to the increasing evidence that there is, in general, no direct link between the long-term insolation-driven changes in the mean climate state and the modes of short-term variability. However, a more complete understanding of Holocene ENSO history would require transient simulations that isolate the different forcings over the Holocene.

5.2. Spatial change of ENSO during the holocene

The uncertainty of the var(EP)/var(CP) ratio combines the effect of sampling internal centennial variability in both regions, resulting in large error bars mostly due to EP data (Fig. 4). The reconstructed variations are not statistically significant and should be thus considered with caution. Nevertheless, our analyses of the var(EP)/var(CP) ratio from paleoclimate records are in agreement with insights into ENSO flavours previously obtained from the asymmetry of ENSO anomalies recorded by Peruvian bivalves (Carré et al., 2014). Those results were based on the observation that the E mode produces positively skewed ENSO anomalies in Peru while the C mode produces negatively skewed anomalies (Dewitte et al., 2012). Both approaches suggest a phase dominated by the C mode 6- 7ka following a phase dominated by the E mode. The strong E mode recorded 7-8ka is consistent with an increased frequency of coastal floods in Peru (Carré et al., 2014; Keefer et al., 2003; Rein, 2007). After 5ka, both records indicate contributions of E and C modes similar to modern. The slightly higher var(EP)/var(CP) ratio during the HEM is not incompatible with low ENSO activity during that time but suggests that ENSO variance was even more reduced in the CP box than in the EP box. There is a third type of ENSO event – coastal El Niños – which produce intense SST anomalies close to the South American coast (Echevin et al., 2018; Garreaud, 2019; Takahashi and Martínez, 2019). The impact of these events, localized in coastal Peru, is similar to those produced by E events in this region. The variability recorded in the EP region thus includes the E mode as well as the coastal El Niño mode.

The var(EP)/var(CP) ratio show different trends in the four transient simulations over the past 6000 years (Fig. 4), using E and C indices calculated from rotated principal components of SST anomalies as defined by Takahashi et al. (2011), report a decreasing (increasing) trend in the C (E) index interannual variability in the CCSM4 model. The proportion of C events was also slightly higher in the mid-Holocene in PMIP2 and PMIP3 simulation ensembles, although strong changes were observed from one model version to the next (An and Choi, 2014). These definitions of ENSO flavours are somewhat different from the ratio used here. We found a slight difference in the IPSL simulations when using the variability of E and C indices instead of the variability in the EP and CP regions as done here (not shown). Therefore, the var(EP)/var(CP) ratio and the var(E)/var(C) ratio, while well correlated in the instrumental record (Fig. 2), seem to represent slightly differently the spatial changes of ENSO in the last 6000 years in the models, possibly due to the representation of the easternmost tropical Pacific. In observations, the variability of the EP region is likely influenced by coastal Niño events and by the dynamic of the coastal upwelling, while the CP region may not reflect well enough the variability further west. Changes in ENSO flavours since the mid-Holocene are not robust across models, and thus provide no evidence of forced changes. While imperfect, the var(EP)/var(CP) ratio estimated from marine records seems a promising approach to examine changes in the spatial expression of ENSO, provided the uncertainty can be reduced, in particular by increasing the dataset in the eastern Pacific.

5.3. ENSO and the annual cycle

The close relationship between ENSO and the annual cycle is shown by the well-documented phase locking of ENSO (An and Choi, 2009; Galanti and Tziperman, 2000; Tziperman et al., 1995; 1998), but theoretical attempts to describe their interaction have not been clearly backed up by observations. Emile-Geay et al. (2016), considering the Pacific as a whole, found a negative correlation between seasonality and ENSO variability in simulations, in line with earlier model studies (An et al., 2010; An and Choi, 2013; Timmermann et al., 2007), in contrast with the positive relationship documented by observations. However most simulations produce both reduced seasonality and reduced interannual variability in the East Pacific (Masson-Delmotte et al., 2013). Hence, the relationship determined for the tropical Pacific as a whole may not be valid for the different regions of the Pacific.

The annual cycle of SSTs in the mid-Holocene in the transient simulations is reduced in the equatorial Pacific, as it was in PMIP2 and PMIP3 mid-Holocene experiments (An and Choi, 2014), and increases progressively in response to orbital forcing. This trend is not observed in paleoclimate data, where the annual cycle of SST has a high millennial scale variability that does not follow the precessional trend (Fig. 3). A positive correlation between seasonality and ENSO variability is found in observations across the Holocene most clearly in the EP regions, and to a lesser extent in the other regions. The relationship is statistically significant only in WP and EP (Fig. 10). The simulated relationship between the amplitude of the annual cycle and the interannual variability of ENSO through time, and separately for different models and different regions, is also mostly positive except in the CP region where both positive and negative relationships are found (Fig. 10). Thus, the negative simulated relationship found by Emile-Geay et al. (2016) is only apparent. The difference with the results presented here likely reflects the stronger representation of regions from the southern hemisphere in our analyses. Calculations of the relationships between simulated interannual variability and for 100-yr windows within successive 2000-yr time slots minimizes the influence of insolation and makes the influence of internal dynamics more apparent (Fig. 11). Among the 130 regressions, only 88 are positive (68 %), of which only 29 are statistically significant. 10 out of the 42 negative regressions are statistically significant. The proportion of positive regressions is highest in the northern region (88 % in the CP) and in the equatorial region (77 % in Niño3.4). The positive relationship is thus relatively robust in the equatorial central Pacific, suggesting that the dynamical link between ENSO and the

annual cycle in models works at multidecadal to orbital timescales.

A negative relationship between the amplitude of the annual cycle and of ENSO was predicted by the frequency entrainment theory which states that ENSO would lose its intrinsic oscillating mode and be suppressed when the strength of the annual forcing increases (Chang et al., 1994; Tziperman et al., 1994; Liu, 2002; Stein et al., 2014). This theory is not supported by paleoclimate observations nor by transient simulations.

5.4. The South West Pacific during the holocene

The most striking feature of the SWP record is the anti-phasing

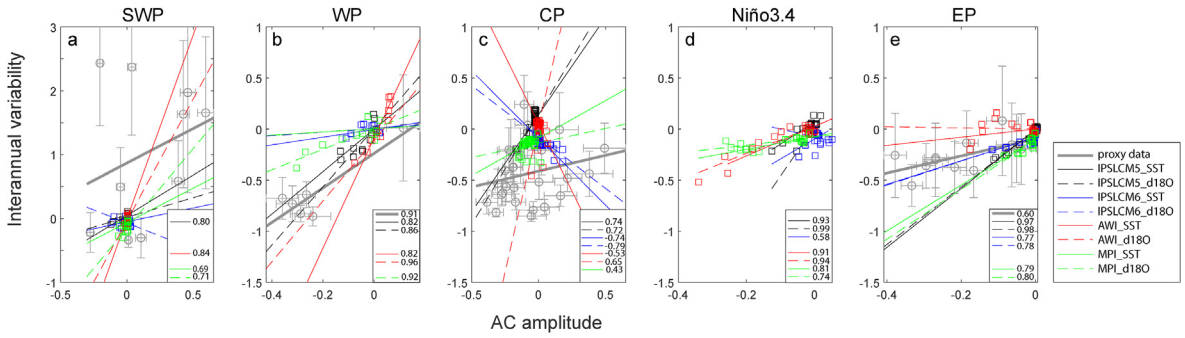

Fig. 10. Regional regressions between interannual variability and Seasonality in models and observations. Interannual variability is plotted versus the amplitude of the annual cycle for individual proxy records (grey circles) in each proxy region, together with values calculated in successive 1000-yr windows in the Holocene for IPSLCM5 (black squares), IPSLCM6 (blue squares), AWI (red squares), and MPI (green squares) models. Linear regressions are shown for proxy records (thick grey lines), modelled SST (thin lines), and pseudo-$\delta^{18}O$ (dashed lines). Boxes in the bottom right indicate regressions that are statistically significant at the 0.05 level and the associated correlation. (For interpretation of the references to colour in this figure legend, the reader is referred to the Web version of this article.)

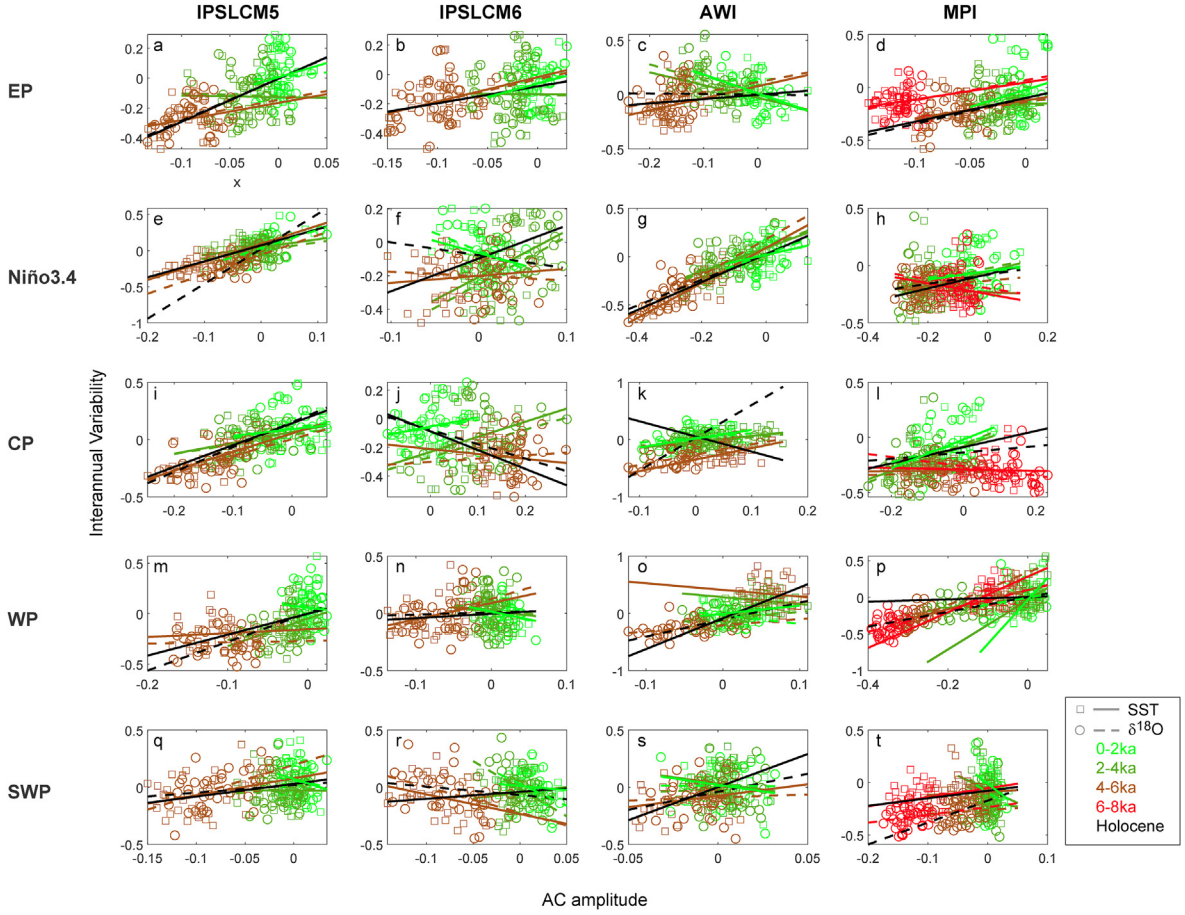

Fig. 11. Regressions between interannual variability and seasonality in models per region and per 2000-yr time slot. Subplots in column 1 to 4 refer to models IPSLCM5, IPSLCM6, AWI and MPI respectively. Subplots in line 1 to 5 correspond to the EP, Niño3.4, CP, WP and SWP regions respectively. Datapoints correspond to SST (squares) and pseudo- $\delta^{18}O$ (circles) in successive 100-year windows from the 0-2ka (green), 2-4ka (light brown), 4-6ka (dark brown), and 6-8ka (red) time slots. Linear regressions are shown for each time slot for SST (continuous lines) and for pseudo- $\delta^{18}O$ (dashed lines), and for the whole period (black). (For interpretation of the references to colour in this figure legend, the reader is referred to the Web version of this article.)

with other regions, particularly the significant increase (~200 %) of interannual variability between 6-4ka when interannual variability is at a minimum in the CP and EP regions (Fig. 3). High variability in the SWP during the mid-Holocene has been identified before and was attributed to ENSO (Corrège et al., 2000). The SWP region is located in the southern part of the South Pacific Convergence Zone (SPCZ) where modern variability is mostly dictated by northward and southward shifts in the SPCZ during El Niño and La Niña events respectively (Folland et al., 2002). However, the high variability in the SWP in the mid-Holocene cannot be an ENSO signal if ENSO was weaker than today in the equatorial Pacific. Nor can it be explained by a change in ENSO flavour since neither the CP events nor the EP events are characterized by larger anomalies in SWP compared to equatorial Pacific. Consequently, it must correspond to another mode of variability, either only weakly expressed in the instrumental record or masked by the ENSO mode. Empirical orthogonal functions (EOF) of SST anomalies (SSTa) correspond to the spatial pattern associated to the principal components of SSTa variability. While the EP and CP modes of ENSO can be described by the first and second EOFs of instrumental SSTa in the tropical Pacific (Ashok et al., 2007; Takahashi et al., 2011), the third EOF is a non-dominant pattern of variability characterized by largest anomalies in the SWP (Ashok et al., 2007). Thus, we hypothesize that the large interannual variability observed in SWP records could correspond to the 3rd EOF of the instrumental SSTa, that might have become more significant when the 1st and 2nd EOFs (i.e. ENSO) were dampened during the HEM.

Additional insights come from comparing the Sr/Ca and $\delta^{18}O$ records from the SWP, to identify the influence of changes in sea water $\delta^{18}O$, closely linked to salinity (Corrège et al., 2004; Duprey et al., 2012). While modern rainfall occurs during the warm season, mid-Holocene corals indicate cooler and saltier mean conditions and precipitation occurring predominantly during the cold season (Duprey et al., 2012). The SWP region was thus not under the influence of the SPCZ, which was located further north in the mid-Holocene (Lazareth et al., 2013), modifying the SPCZ-ENSO relationship. This explains why interannual variability estimates were not amplified by $\delta^{18}O$ records compared to Sr/Ca in the SWP (Fig. 8), as would be expected in tropical regions where temperature and precipitation are associated (Thompson et al., 2011). Our result supports a previous multi-model study showing that changes in the SPCZ interannual variability are independent of changes in ENSO amplitude, both through orbital changes and between models, although there is a robust response to mid-Holocene insolation characterised by reduced ENSO variability and a DJF southward shift of the SPCZ mean position (Saint-Lu et al., 2015).

Model biases in the representation of the SPCZ preclude a reliable assessment of past variability and rainfall regime in the SWP region. However, an increase of the frequency and amplitude of the SPCZ interannual latitudinal shifts at 6ka is simulated in the IPSL-CM5 model, although ENSO was weakened (Saint-Lu et al., 2015), in agreement with our data synthesis. The Holocene paleoclimate observation and simulations support predictions of larger shifts in the SPCZ in a greenhouse climate although models do not agree on future changes in ENSO variability (Cai et al., 2012).

6. Summary and conclusions

We have quantified millennial-scale changes in the amplitude of the annual cycle and the interannual variability in four regions of the Pacific based on a new synthesis of seasonally resolved $\delta^{18}O$ and Sr/Ca Holocene coral and bivalve records from the tropical Pacific (Fig. 1). The uncertainty due to the sampling of internal climate variability by short records was estimated for an objective comparison with four transient climate simulations. Observations confirm the HEM in the EP and CP with reductions in ENSO variance of ~50 % and ~80 % respectively. While ENSO variance 6-8ka was not significantly different from the late Holocene in EP and CP, there is an 85 % reduction in WP, possibly amplified by changes in hydroclimate, as suggested by simulations and Sr/Ca data. Models and data generally agree on a positive relationship between the amplitude of the annual cycle and ENSO variance, especially in the EP. Changes in the ratio of ENSO variance in the EP and CP regions, var(EP)/var(CP), suggest possible changes in the spatial pattern of ENSO during the Holocene, consistent with previous evidence (Carré et al., 2014), although this needs confirmation from additional data. Interannual variability in the SWP increases by 200 % between 4-6ka, in antiphase with the ENSO variability minimum recorded in the equatorial Pacific. This implies that the SWP interannual variability was associated to another mode of variability during this period. Cooler, saltier conditions and winter precipitation indicate that the region was not under the influence of the SPCZ at this time. The change in ENSO variance after 6ka can be robustly attributed to insolation forcing using CP records and the insolation forced transient simulations. ENSO sensitivity to orbital forcing is, however, underestimated in models by a factor of 4.7 compared to data. Millennial-scale unforced variability of ENSO is apparent in both observations and models and might partly account for the amplitude of the HEM. Insolation forcing of ENSO is not incompatible with high variance in the early Holocene, when other competing mechanisms were at play. Despite significant advances, our understanding of ENSO during the Holocene is still limited by the number of fossil records. An increased effort in data acquisition is particularly needed in the Eastern and Western Pacific.

Author statement

Matthieu Carré, Pascale Braconnot, Mary Elliot, Thierry Corrège and Sandy P. Harrison conceptualized the study and developed the methodology; Matthieu Carré and Rachid Cheddadi were responsible for data curation; Pascale Braconnot, Olivier Marti, Xiaoxu Shi, Roberta d'Agostino, Gerrit Lohmann and Johann Jungclaus contributed to the model simulations and their analysis; Matthieu Carré wrote the Matlab codes, did the formal analyses, and wrote the draft manuscript; Andrew Schurer validated the detection attribution analysis; Pascale Braconnot and Isma Abdelkader di Carlo validated the ENSO flavour analysis; Pascale Braconnot, Matthieu Carré, Bruno Turcq, Thierry Corrège, Sandy P. Harrison, Gerrit Lohmann, Johann Jungclaus, and Jorge Cardich contributed to funding acquisition. All authors contributed to the preparation of the manuscript.

Data and code availability

The complete PACMEDY_Coral&Bivalve_database is available at https://doi.org/10.6084/m9.figshare.14256434.

The Pacific synthesis extracted from this database, the interannual variability and seasonality values calculated from proxy records and simulations, as well as the Matlab scripts for analyses and figures are available in a public repository at https://doi.org/10.6084/m9.figshare.14273381.

Funding

This research has been supported by the JPI-Belmont project PACMEDY (via grant ANR-15-JCLI-0003-01 for MC, PB, ME, OM, TC, and BT). MC, JC, DO, RSG, AP, and PR acknowledge funding from Concejo Nacional de Ciencia y Tecnologia de Peru (grant n° 007-2017-FONDECYT, grant n° 034-2019-FONDECYT-BM). SPH

acknowledges funding from the ERC-funded project GC2.0Global Change 2.0: Unlocking the past for a clearer future, grant number 694481and from the JPI-Belmont project PACMEDY (via NERC). The distribution and analyses of the transient Holocene simulations with the IPSL model benefit from the Institut Pierre Simon Laplace Climate Modeling Centre Infrastructure supported by ANR "Investissements d'avenir" program ANR-11-IDEX-0004-17-EURE-0006.

Declaration of competing interest

The authors declare that they have no known competing financial interests or personal relationships that could have appeared to influence the work reported in this paper.

Acknowledgements

We acknowledge the modelling groups of Institut Pierre Simon Laplace, Alfred Wegener Institute and Max Planck Institute for producing and sharing the climate simulations. We are thankful to all the authors who produced the paleoclimate records gathered in this paper for making their data public or sharing them with us. This research was funded by the JPI-Belmont Forum project entitled Palaeo-climate Constraints on Monsoon Evolution and Dynamics (PACMEDY). We thank two anonymous reviewers for their constructive comments.

References

An, S.-I., Choi, J., 2013. Inverse relationship between the equatorial eastern Pacific annual-cycle and ENSO amplitudes in a coupled general circulation model. Clim. Dynam. 40, 663–675. https://doi.org/10.1007/s00382-012-1403-3.

An, S.-I., Choi, J., 2014. Mid-Holocene tropical Pacific climate state, annual cycle, and ENSO in PMIP2 and PMIP3. Clim. Dynam. 43, 957–970. https://doi.org/10.1007/s00382-013-1880-z.

An, S.I., Choi, J., 2009. Seasonal locking of the ENSO asymmetry and its influence on the seasonal cycle of the tropical eastern Pacific sea surface temperature. Atmos. Res. 94, 3–9.

An, S.-I., Ham, Y.-G., Kug, J.-S., Timmermann, A., Choi, J., Kang, I.-S., 2010. The Inverse Effect of Annual-Mean State and Annual-Cycle Changes on ENSO. J. Clim. 23, 1095–1110. https://doi.org/10.1175/2009JCLI2895.1.

Arntz, W.E., Brey, T., Tarazona, J., Robles, A., 1987. Changes in the structure of a shallow sandy-beach community in Peru during an El Niño event. In: Payne, A.I.L., Gulland, J.A., Brinks, K.H. (Eds.), The Benguela and Comparable Ecosystems. South African Journal of Marine Science, pp. 645–658.

Ashok, K., Behera, S.K., Rao, S.A., Weng, H., Yamagata, T., 2007. El Niño modoki and its possible teleconnection. J. Geophys. Res. 112, C11007. https://doi.org/10.1029/2006JC003798.

Bader, J., Jungclaus, J., Krivova, N., Lorenz, S., Maycock, A., Raddatz, T., Schmidt, H., Toohey, M., Wu, C.-J., Claussen, M., 2020. Global temperature modes shed light on the Holocene temperature conundrum. Nat. Commun. 11, 4726. https://doi.org/10.1038/s41467-020-18478-6.

Bard, E., Hamelin, B., Arnold, M., Montaggioni, L., Cabioch, G., Faure, G., Rougerie, F., 1996. Deglacial sa-level record from Tahiti corals and the timing of global meltwater discharge. Nature 382, 241–244.

Bartlein, P.J., Shafer, S.L., 2019. Paleo calendar-effect adjustments in time-slice and transient climate-model simulations (PaleoCalAdjust v1.0): impact and strategies for data analysis. Geosci. Model Dev. (GMD) 12, 3889–3913. https://doi.org/10.5194/gmd-12-3889-2019.

Beck, J.W., Edwards, R.L., Ito, E., Taylor, F.W., Recy, J., Rougerie, F., Joannot, P., Henin, C., 1992. Sea-surface temperature from coral skeletal Strontium/Calcium ratios. Science 257, 644–647.

Beck, J.W., Récy, J., Taylor, F., Edwards, R.L., Cabioch, G., 1997. Abrupt changes in early Holocene tropical sea surface temperature derived from coral records. Nature 385, 705–707. https://doi.org/10.1038/385705a0.

Bellenger, H., Guilyardi, E., Leloup, J., Lengaigne, M., Vialard, J., 2014. ENSO representation in climate models: from CMIP3 to CMIP5. Clim. Dynam. 42, 1999–2018. https://doi.org/10.1007/s00382-013-1783-z.

Berger, A., 1978. Long-term variations of caloric insolation resulting from the earth's orbital elements. Quat. Res. 9, 139–167.

Boucher, O., Servonnat, J., Albright, A.L., Aumont, O., Balkanski, Y., Bastrikov, V., Bekki, S., Bonnet, R., Bony, S., Bopp, L., Braconnot, P., Brockmann, P., Cadule, P., Caubel, A., Cheruy, F., Codron, F., Cozic, A., Cugnet, D., D'Andrea, F., Davini, P., de Lavergne, C., Denvil, S., Deshayes, J., Devilliers, M., Ducharne, A., Dufresne, J.-L., Dupont, E., Éthé, C., Fairhead, L., Falletti, L., Flavoni, S., Foujols, M.-A., Gardoll, S., Gastineau, G., Ghattas, J., Grandpeix, J.-Y., Guenet, B., Guez, L.E., Guilyardi, E., Guimberteau, M., Hauglustaine, D., Hourdin, F., Idelkadi, A., Joussaume, S., Kageyama, M., Khodri, M., Krinner, G., Lebas, N., Levavasseur, G., Lévy, C., Li, L., Lott, F., Lurton, T., Luyssaert, S., Madec, G., Madeleine, J.-B., Maignan, F., Marchand, M., Marti, O., Mellul, L., Meurdesoif, Y., Mignot, J., Musat, I., Ottlé, C., Peylin, P., Planton, Y., Polcher, J., Rio, C., Rochetin, N., Rousset, C., Sepulchre, P., Sima, A., Swingedouw, D., Thiéblemont, R., Traore, A.K., Vancoppenolle, M., Vial, J., Vialard, J., Viovy, N., Vuichard, N., 2020. Presentation and evaluation of the IPSL-CM6A-LR climate model. J. Adv. Model. Earth Syst. 12. https://doi.org/10.1029/2019MS002010 e2019MS002010.

Braconnot, P., Crétat, J., Marti, O., Balkanski, Y., Caubel, A., Cozic, A., Foujols, M.-A., Sanogo, S., 2019a. Impact of multiscale variability on last 6,000 Years Indian and West african monsoon rain. Geophys. Res. Lett. 46, 14021–14029. https://doi.org/10.1029/2019GL084797.

Braconnot, P., Harrison, S.P., Kageyama, M., Bartlein, P.J., Masson-Delmotte, V., Abe-Ouchi, A., Otto-Bliesner, B., Zhao, Y., 2012a. Evaluation of climate models using palaeoclimatic data. Nature Clim. Change 2, 417–424.

Braconnot, P., Luan, Y., Brewer, S., Zheng, W., 2012b. Impact of Earth's orbit and freshwater fluxes on Holocene climate mean seasonal cycle and ENSO characteristics. Clim. Dynam. 38, 1081–1092.

Braconnot, P., Otto-Bliesner, B., Harrison, S., Jousseaume, S., Peterschmitt, J.-Y., Abe-Ouchi, A., Crucifix, M., Driesschaert, E., Fichefet, T., Hewitt, C.D., Kageyama, M., Kitoh, A., Loutre, M.F., Marti, O., Merkel, U., Ramstein, G., Valdes, P., Weber, S.L., Yu, Y., Zhao, Y., 2007. Results of PMIP2 coupled simulations of the Mid-Holocene and Last Glacial Maximum-Part2: feedbacks with emphasis o nthe location of the ITCZ and mid- and high latitudes heat budget. Clim. Past 3, 279–296.

Braconnot, P., Zhu, D., Marti, O., Servonnat, J., 2019b. Strengths and challenges for transient Mid- to Late Holocene simulations with dynamical vegetation. Clim. Past 15, 997–1024.

Brown, J., Tudhope, A.W., Collins, M., McGregor, H.V., 2008a. Mid-Holocene ENSO: issues in quantitative model-proxy data comparisons. Paleoceanography 23. https://doi.org/10.1029/2007PA001512.

Brown, J.R., Brierley, C.M., An, S.-I., Guarino, M.-V., Stevenson, S., Williams, C.J.R., Zhang, Q., Zhao, A., Abe-Ouchi, A., Braconnot, P., Brady, E.C., Chandan, D., D'Agostino, R., Guo, C., LeGrande, A.N., Lohmann, G., Morozova, P.A., Ohgaito, R., O'ishi, R., Otto-Bliesner, B.L., Peltier, W.R., Shi, X., Sime, L., Volodin, E.M., Zhang, Z., Zheng, W., 2020. Comparison of past and future simulations of ENSO in CMIP5/PMIP3 and CMIP6/PMIP4 models. Clim. Past 16, 1777–1805. https://doi.org/10.5194/cp-16-1777-2020.

Brown, J.R., Collins, M., Tudhope, A., Toniazzo, T., 2008b. Modelling mid-Holocene tropical climate and ENSO variability: towards constraining predictions of future change with palaeo-data. Clim. Dynam. 30, 19–36.

Cai, W., Lengaigne, M., Borlace, S., Collins, M., Cowan, T., McPhaden, M.J., Timmermann, A., Power, S., Brown, J., Menkes, C., Ngari, A., Vincent, E.M., Widlansky, M.J., 2012. More extreme swings of the South Pacific convergence zone due to greenhouse warming. Nature 488, 365–369.

Carré, M., Bentaleb, I., Blamart, D., Ogle, N., Cardenas, F., Zevallos, S., Kalin, R.M., Ortlieb, L., Fontugne, M., 2005a. Stable isotopes and sclerochronology of the bivalve Mesodesma donacium: potential application to peruvian paleoceanographic reconstructions. Palaeogeography, Palaeoclimatology. Palaeoecology 228, 4–25.

Carré, M., Bentaleb, I., Fontugne, M., Lavallée, D., 2005b. Strong El Niño events during the early Holocene: stable isotope evidence from Peruvian sea-shells. Holocene 15, 42–47.

Carré, M., Cheddadi, R., 2017. Seasonality in long-term climate change. Quaternaire 28, 173–177. https://doi.org/10.4000/quaternaire.8018.

Carré, M., Elliot, M., Corrège, T., Harrison, S.P., Braconnot, P., 2021. PACMEDY Coral&Bivalve Database_v1.

Carré, M., Sachs, J.P., Purca, S., Schauer, A.J., Braconnot, P., Angeles Falcón, R., Julien, M., Lavallée, D., 2014. Holocene history of ENSO variance and asymmetry in the eastern tropical Pacific. Science 345, 1045–1048. https://doi.org/10.1126/science.1252220.

Carré, M., Sachs, J.P., Schauer, A.J., Rodríguez, W.E., Ramos, F.C., 2013. Reconstructing El Niño-Southern Oscillation activity and ocean temperature seasonality from short-lived marine mollusk shells from Peru. Palaeogeography, Palaeoclimatology. Palaeoecology 371, 45–53.

Carré, M., Sachs, J.P., Wallace, J.M., Favier, C., 2012a. Exploring errors in paleoclimate proxy reconstructions using Monte Carlo simulations: paleotemperature from mollusk and coral geochemistry. Clim. Past 8, 433–450. https://doi.org/10.5194/cp-8-433-2012.

Carré, M., Azzoug, M., Bentaleb, I., Chase, B.M., Fontugne, M., Jackson, D., Ledru, M.-P., Maldonado, A., Sachs, J.P., Schauer, A.J., 2012b. Mid-Holocene mean climate in the south-eastern Pacific and its influence on South America. Quat. Int. 253, 55–66. https://doi.org/10.1016/j.quaint.2011.02.004.

Chang, P., Wang, B., Li, T., Ji, L., 1994. Interactions between the seasonal cycle and the southern oscillation - frequency entrainment and chaos in a coupled ocean-atmosphere model. Geophys. Res. Lett. 21, 2817–2820.

Chappell, J., Polach, H., 1991. Post-glacial sea-level rise from a coral record at Huon Peninsula, Papua New Guinea. Nature 349, 147–149. https://doi.org/10.1038/349147a0.

Cheddadi, R., Carré, M., Nourelbait, M., François, L., Rhoujjati, A., Manay, R., Ochoa, D., Schefuß, E., 2021. Early Holocene greening of the Sahara requires Mediterranean winter rainfall. Proc. Natl. Acad. Sci. Unit. States Am. 118. https://doi.org/10.1073/pnas.2024898118.

Chen, S., Hoffmann, S.S., Lund, D.C., Cobb, K.M., Emile-Geay, J., Adkins, J.F., 2016. A high-resolution speleothem record of western equatorial Pacific rainfall: implications for Holocene ENSO evolution. Earth Planet Sci. Lett. 442, 61–71.

Clement, A.C., Seager, R., Cane, M.A., 2000. Suppression of El Niño during the mid-Holocene by changes in earth's orbit. Paleoceanography 15, 731–737.
Clement, A.C., Seager, R., Cane, M.A., 1999. Orbital controls on the el niño/southern oscillation and the tropical climate. Paleoceanography 14, 441–456.
Cobb, K.M., Charles, C.D., Cheng, H., Edwards, R.L., 2003. El Niño/Southern Oscillation and tropical Pacific climate during the last millennium. Nature 424, 271–276.
Cobb, K.M., Westphal, N., Sayani, H.R., Watson, J.T., Di Lorenzo, E., Cheng, H., Edwards, R.L., Charles, C.D., 2013. Highly variable el niño-southern oscillation throughout the Holocene. Science 339, 67–70. https://doi.org/10.1126/science.1228246.
Cole, J.E., Fairbanks, R.G., Shen, G.T., 1993. Recent variability in the southern oscillation: isotopic results from a tarawa atoll coral. Science 260, 1790–1793.
Conroy, J.L., Cobb, K.M., Lynch-Stieglitz, J., Polissar, P.J., 2014. Constraints on the salinity-oxygen isotope relationship in the central tropical Pacific Ocean. Mar. Chem. (in press).
Conroy, J.L., Overpeck, J.T., Cole, J.E., Shanahan, T.M., Steinitz-Kannan, M., 2008. Holocene changes in eastern Pacific climate inferred from a Galápagos lake sediment record. Quat. Sci. Rev. 27, 1166–1180.
Conroy, J.L., Thompson, D.M., Cobb, K.M., Noone, D., Rea, S., Legrande, A.N.C.P.A., 2017. Spatiotemporal variability in the δ18O-salinity relationship of seawater across the tropical Pacific Ocean. Paleoceanography 32, 484–497. https://doi.org/10.1002/2016PA003073.
Corrège, T., Delcroix, T., Rècy, J., Beck, W., Cabioch, G., Le Cornec, F., 2000. Evidence for stronger el niño-southern oscillation (ENSO) events in a mid-holocene massive coral. Paleoceanography 15, 465–470.
Corrège, T., Gagan, M.K., Beck, J.W., Burr, G.S., Cabioch, G., Le Cornec, F., 2004. Interdecadal variation in the extent of South Pacific tropical waters during the Younger Dryas event. Nature 428, 927–929.
Crétat, J., Braconnot, P., Terray, P., Marti, O., Falasca, F., 2020. Mid-Holocene to present-day evolution of the Indian monsoon in transient global simulations. Clim. Dynam. 55, 2761–2784. https://doi.org/10.1007/s00382-020-05418-9.
Cruz, F.W., Vuille, M., Burns, S.J., Wang, X., Cheng, H., Werner, M., Lawrence Edwards, R., Karmann, I., Auler, A.S., Nguyen, H., 2009. Orbitally driven east–west antiphasing of South American precipitation. Nat. Geosci. 2, 210–214. https://doi.org/10.1038/ngeo444.
D'Agostino, R., Bader, J., Bordoni, S., Ferreira, D., Jungclaus, J., 2019. Northern hemisphere monsoon response to mid-holocene orbital forcing and greenhouse gas-induced global warming. Geophys. Res. Lett. 46, 1591–1601. https://doi.org/10.1029/2018GL081589.
D'Agostino, R., Brown, J.R., Moise, A., Nguyen, H., Dias, P.L.S., Jungclaus, J., 2020. Contrasting southern hemisphere monsoon response: MidHolocene orbital forcing versus future greenhouse gas–induced global warming. J. Clim. 33, 9595–9613. https://doi.org/10.1175/JCLI-D-19-0672.1.
Dallmeyer, A., Claussen, M., Lorenz, S.J., Shanahan, T., 2020. The end of the African humid period as seen by a transient comprehensive Earth system model simulation of the last 8000 years. Clim. Past 16, 117–140. https://doi.org/10.5194/cp-16-117-2020.
Danilov, S., Sidorenko, D., Wang, Q., Jung, T., 2017. The finite-volumE sea ice–ocean model (FESOM2). Geosci. Model Dev. (GMD) 10, 765–789. https://doi.org/10.5194/gmd-10-765-2017.
DeLong, K.L., Quinn, T.M., Taylor, F.W., Shen, C.-C., Lin, K., 2013. Improving coral-base paleoclimate reconstructions by replicating 350years of coral Sr/Ca variations. Palaeogeogr. Palaeoclimatol. Palaeoecol. 373, 6–24. https://doi.org/10.1016/j.palaeo.2012.08.019.
DelSole, T., Trenary, L., Yan, X., Tippett, M.K., 2019. Confidence intervals in optimal fingerprinting. Clim. Dynam. 52, 4111–4126. https://doi.org/10.1007/s00382-018-4356-3.
Dewitte, B., Vazquez-Cuervo, J., Goubanova, K., Illig, S., Takahashi, K., Cambon, G., Purca, S., Correa, D., Gutierrez, D., Sifeddine, A., Ortlieb, L., 2012. Change in El Niño flavours over 1958-2008: implications for the long-term trend of the upwelling off Peru. Deep Sea Res. Part II Top. Stud. Oceanogr. 77–80, 143–156.
Dong, B., Sutton, R.T., 2007. Enhancement of ENSO variability by a weakened Atlantic thermohaline circulation in a coupled GCM. J. Clim. 20, 4920–4939.
Driscoll, R., Elliot, M., Russon, T., Welsh, K., Yokoyama, Y., Tudhope, A., 2014. ENSO reconstructions over the past 60 ka using giant clams (Tridacna sp.) from Papua New Guinea. Geophys. Res. Lett. 41, 2014GL061446.
Dufresne, J.-L., Foujols, M.-A., Denvil, S., Caubel, A., Marti, O., Aumont, O., Balkanski, Y., Bekki, S., Bellenger, H., Benshila, R., Bony, S., Bopp, L., Braconnot, P., Brockmann, P., Cadule, P., Cheruy, F., Codron, F., Cozic, A., Cugnet, D., de Noblet, N., Duvel, J.-P., Ethé, C., Fairhead, L., Fichefet, T., Flavoni, S., Friedlingstein, P., Grandpeix, J.-Y., Guez, L., Guilyardi, E., Hauglustaine, D., Hourdin, F., Idelkadi, A., Ghattas, J., Joussaume, S., Kageyama, M., Krinner, G., Labetoulle, S., Lahellec, A., Lefebvre, M.-P., Lefevre, F., Levy, C., Li, Z.X., Lloyd, J., Lott, F., Madec, G., Mancip, M., Marchand, M., Masson, S., Meurdesoif, Y., Mignot, J., Musat, I., Parouty, S., Polcher, J., Rio, C., Schulz, M., Swingedouw, D., Szopa, S., Talandier, C., Terray, P., Viovy, N., Vuichard, N., 2013. Climate change projections using the IPSL-CM5 earth system model: from CMIP3 to CMIP5. Clim. Dynam. 40, 2123–2165. https://doi.org/10.1007/s00382-012-1636-1.
Duprey, N., Lazareth, C.E., Corrège, T., Le Cornec, F., Maes, C., Pujol, N., Madeng-Yogo, M., Caquineau, S., Soares Derome, C., Cabioch, G., 2012. Early mid-Holocene SST variability and surface-ocean water balance in the southwest Pacific. Paleoceanography 27, PA4207.
Echevin, V., Colas, F., Espinoza-Morriberon, D., Vasquez, L., Anculle, T., Gutierrez, D., 2018. Forcings and evolution of the 2017 coastal el Niño off northern Peru and Ecuador. Frontiers in Marine Science 5 (367). https://doi.org/10.3389/fmars.2018.00367.
Emile-Geay, J., Cobb, K.M., Carre, M., Braconnot, P., Leloup, J., Zhou, Y., Harrison, S.P., Correge, T., McGregor, H.V., Collins, M., Driscoll, R., Elliot, M., Schneider, B., Tudhope, A., 2016. Links between tropical Pacific seasonal, interannual and orbital variability during the Holocene. Nat. Geosci. 9, 168–173. https://doi.org/10.1038/ngeo2608.
Emile-Geay, J., Cobb, K.M., Cole, J.E., Elliot, M., Zhu, F., 2020. Past ENSO variability. In: McPhaden, M.J., Santoso, A., Cai, W. (Eds.), El Niño Southern Oscillation in a Changing Climate, Geophysical Monograph Series.
Evans, M.N., Kaplan, A., Cane, M.A., 2000. Intercomparison of coral oxygen isotope data and historical sea surface temperature (SST): potential for coral-based SST field reconstructions. Paleoceanography 15, 551–563. https://doi.org/10.1029/2000PA000498.
Fairbanks, R.G., Charles, C.D., Wright, J.D., 1992. Origin of global meltwater pulses. In: Taylor, R.E., et al. (Eds.), Radiocarbon after Four Decads:Springer-Verlag, pp. 473–500.
Folland, C.K., Renwick, J.A., Salinger, M.J., Mullan, A.B., 2002. Relative influences of the interdecadal pacific oscillation and ENSO on the south pacific convergence zone. Geophys. Res. Lett. 29. https://doi.org/10.1029/2001GL014201, 21–1.
Gagan, M.K., Dunbar, G.B., Suzuki, A., 2012. The effect of skeletal mass accumulation in Porites on coral Sr/Ca and δ18O paleothermometry. Paleoceanography 27. https://doi.org/10.1029/2011PA002215.
Galanti, E., Tziperman, E., 2000. ENSO's phase locking to the seasonal cycle in the fast-SST, fast-wave, and mixed-mode regimes. J. Clim. 57, 2936–2950.
Garreaud, R.D., 2019. A plausible atmospheric trigger for the 2017 coastal El Niño. Int. J. Climatol. 38, e1296–e1302.
Giorgetta, M.A., Jungclaus, J., Reick, C.H., Legutke, S., Bader, J., Böttinger, M., Brovkin, V., Crueger, T., Esch, M., Fieg, K., Glushak, K., Gayler, V., Haak, H., Hollweg, H.-D., Ilyina, T., Kinne, S., Kornblueh, L., Matei, D., Mauritsen, T., Mikolajewicz, U., Mueller, W., Notz, D., Pithan, F., Raddatz, T., Rast, S., Redler, R., Roeckner, E., Schmidt, H., Schnur, R., Segschneider, J., Six, K.D., Stockhause, M., Timmreck, C., Wegner, J., Widmann, H., Wieners, K.-H., Claussen, M., Marotzke, J., Stevens, B., 2013. Climate and carbon cycle changes from 1850 to 2100 in MPI-ESM simulations for the Coupled Model Intercomparison Project phase 5. J. Adv. Model. Earth Syst. 5, 572–597. https://doi.org/10.1002/jame.20038.
Glynn, P.W., Maté, J.L., Baker, A.C., Calderón, M.O., 2001. Coral bleaching and mortality in Panama and Ecuador during the 1997–1998 El Niño–Southern Oscillation Event: spatial/temporal patterns and comparisons with the 1982–1983 event. Bull. Mar. Sci. 69, 79–109.
Goodbred Jr., S.L., Kuehl, S.A., 2000. Enormous Ganges-Brahmaputra sediment discharge during strengthened early Holocene monsoon. Geology 28, 1083–1086. https://doi.org/10.1130/0091-7613(2000)28<1083:EGSDDS>2.0.CO;2.
Grossman, E.E., Fletcher III, C.H., Richmond, B.M., 1998. The Holocene sea-level highstand in the equatorial Pacific: analysis of the insular paleosea-level database. Coral Reefs 17, 309–327.
Grossman, E.L., Ku, T.-L., 1986. Oxygen and carbon fractionation in biogenic aragonite: temperature effect. Chem. Geol. 59, 59–74.
Harrison, S.P., Bartlein, P.J., Izumi, K., Li, G., Annan, J., Hargreaves, J., Braconnot, P., Kageyama, M., 2015. Evaluation of CMIP5 palaeo-simulations to improve climate projections. Nature Clim. Change 5, 735–743.
Haug, G.H., Hughen, K.A., Sigman, D.M., Peterson, L.C., Röhl, U., 2001. Southward migration of the intertropical convergence zone through the Holocene. Science 293, 1304–1308.
Hegerl, G., Zwiers, F., 2011. Use of models in detection and attribution of climate change. WIREs Climate Change 2, 570–591. https://doi.org/10.1002/wcc.121.
Huang, B., Thorne, P.W., Banzon, V.F., Boyer, T., Chepurin, G., Lawrimore, J.H., Menne, M.J., Smith, T.M., Vose, R.S., Zhang, H.M., 2017. NOAA Extended Reconstructed Sea Surface Temperature (ERSST). https://doi.org/10.7289/V5T72FNM. NOAA National Centers for Environmental Information., Version 5.
Ilyina, T., Six, K.D., Segschneider, J., Maier-Reimer, E., Li, H., Núñez-Riboni, I., 2013. Global ocean biogeochemistry model HAMOCC: model architecture and performance as component of the MPI-Earth system model in different CMIP5 experimental realizations. J. Adv. Model. Earth Syst. 5, 287–315. https://doi.org/10.1029/2012MS000178.
Joussaume, S., Taylor, K.E., Braconnot, P., Mitchell, J.F.B., Kutzbach, J.E., Harrison, S.P., Prentice, I.C., Broccoli, A.J., Abe-Ouchi, A., Bartlein, P.J., Bonfils, C., Dong, B., Guiot, J., Herterich, K., Hewitt, C.D., Jolly, D., Kim, J.W., Kislov, A., Kitoh, A., Loutre, M.F., Masson, V., McAvaney, B., McFarlane, N., de Noblet, N., Peltier, W.R., Peterscmitt, J.Y., Pollard, D., Rind, D., Royer, J.F., Schlesinger, M.E., Syktus, J., Thompson, S., Valdes, P., Vettoretti, G., Webb, R.S., Wyputta, U., 1999. Monsoon changes for 6000years ago: results of 18 simulations from the paleoclimate modeling intercomparison project (PMIP). Geophys. Res. Lett. 26, 859–862.
Juillet-Leclerc, A., Schmidt, G., 2001. A calibration of the oxygen isotope paleothermometer of coral aragonite from porites. Geophys. Res. Lett. 28, 4135–4138. https://doi.org/10.1029/2000GL012538.
Jungclaus, J.H., Fischer, N., Haak, H., Lohmann, K., Marotzke, J., Matei, D., Mikolajewicz, U., Notz, D., von Storch, J.S., 2013. Characteristics of the ocean simulations in the Max Planck Institute Ocean Model (MPIOM) the ocean component of the MPI-Earth system model. J. Adv. Model. Earth Syst. 5, 422–446. https://doi.org/10.1002/jame.20023.
Kageyama, M., Braconnot, P., Bopp, L., Caubel, A., Foujols, M.-A., Guilyardi, E., Khodri, M., Lloyd, J., Lombard, F., Mariotti, V., Marti, O., Roy, T., Woillez, M.-N.,

2013. Mid-Holocene and Last Glacial Maximum climate simulations with the IPSL model—part I: comparing IPSL_CM5A to IPSL_CM4. Clim. Dynam. 40, 2447–2468. https://doi.org/10.1007/s00382-012-1488-8.
Kageyama, M., Harrison, S.P., Kapsch, M.-L., Lofverstrom, M., Lora, J.M., Mikolajewicz, U., Sherriff-Tadano, S., Vadsaria, T., Abe-Ouchi, A., Bouttes, N., Chandan, D., Gregoire, L.J., Ivanovic, R.F., Izumi, K., LeGrande, A.N., Lhardy, F., Lohmann, G., Morozova, P.A., Ohgaito, R., Paul, A., Peltier, W.R., Poulsen, C.J., Quiquet, A., Roche, D.M., Shi, X., Tierney, J.E., Valdes, P.J., Volodin, E., Zhu, J., 2021. The PMIP4 Last Glacial Maximum experiments: preliminary results and comparison with the PMIP3 simulations. Clim. Past 17, 1065–1089. https://doi.org/10.5194/cp-17-1065-2021.
Kao, H.-Y., Yu, J.-Y., 2009. Contrasting eastern-pacific and central-pacific types of ENSO. J. Clim. 22, 615–632. https://doi.org/10.1175/2008JCLI2309.1.
Karamperidou, C., Di Nezio, P.N., Timmermann, A., Jin, F.-F., Cobb, K.M., 2015. The response of ENSO flavors to mid-Holocene climate: Implications for proxy interpretation. Paleoceanography 30, 527–547. https://doi.org/10.1002/2014PA002742.
Keefer, D.K., Moseley, M.E., deFrance, S.D., 2003. A 38,000-year record of floods and debris flows in the Ilo region of southern Peru and its relation to El Niño events and great earthquakes. Palaeogeogr. Palaeoclimatol. Palaeoecol. 194, 41–77.
Kiefer, J., Karamperidou, C., 2019. High-resolution modeling of ENSO-induced precipitation in the Tropical Andes: implications for proxy interpretation. Paleoceanogr. Paleoclimatol. 34, 217–236.
Kilbourne, K.H., Quinn, T.M., Taylor, F.W., Delcroix, T., Gouriou, Y., 2004. El Niño-Southern Oscillation-related salinity variations recorded in the skeletal geochemistry of a Porites coral from Espiritu Santo, Vanuatu. Paleoceanography 19, PA4002.
Köhler, P., Nehrbass-Ahles, C., Schmitt, J., Stocker, T.F., Fischer, H., 2017. A 156 kyr smoothed history of the atmospheric greenhouse gases CO2, CH4, and N2O and their radiative forcing. Earth Syst. Sci. Data 9, 363–387. https://doi.org/10.5194/essd-9-363-2017.
Koutavas, A., Joanides, S., 2012. El niño–southern oscillation extrema in the Holocene and last glacial maximum. Paleoceanography 27. https://doi.org/10.1029/2012PA002378.
Koutavas, A., Lynch-Stieglitz, J., Marchitto Jr., T.M., Sachs, J.P., 2002. El Niño-like pattern in ice age tropical sea surface temperature. Science 297, 226–230.
Krinner, G., Viovy, N., de Noblet-Ducoudré, N., Ogée, J., Polcher, J., Friedlingstein, P., Ciais, P., Sitch, S., Prentice, I.C., 2005. A dynamic global vegetation model for studies of the coupled atmosphere-biosphere system. Global Biogeochem. Cycles 19. https://doi.org/10.1029/2003GB002199.
Krol, L.R., 2020. Permutation Test.
Kutzbach, J., 1981. Monsoon climate of the early Holocene: climate experiment with the earth's orbital parameters for 9000 Years ago. Science 214 (59). https://doi.org/10.1126/science.214.4516.59.
Lambeck, K., Nakada, M., 1990. Late Pleistocene and Holocene sea-level change along the Australian coast. Palaeogeogr. Palaeoclimatol. Palaeoecol. 89, 143–176. https://doi.org/10.1016/0031-0182(90)90056-D.
Lavallée, D., Julien, M., Béarez, P., Bolaños, A., Carré, M., Chevalier, A., Delabarde, T., Fontugne, M., Rodríguez-Loredo, C., Klaric, L., Usselmann, P., Vanhaeren, M., 2011. Quebrada de los burros. Los primeros pescadores del litoral Pacífico en el extremo sur peruano. Chungara, Revista de Antropología Chilena 43, 333–351.
Lazareth, C.E., Bustamante Rosell, M.G., Turcq, B., Le Cornec, F., Mandeng-Yogo, M., Caquineau, S., Cabioch, G., 2013. Mid-Holocene climate in New Caledonia (southwest Pacific): coral and PMIP models monthly resolved results. Quat. Sci. Rev. 69, 83–97.
Lee, T., McPhaden, M.J., 2010. Increasing intensity of el Niño in the central-equatorial pacific. Geophys. Res. Lett. 37, L14603.
LeGrande, A.N., Schmidt, G.A., 2011. Water isotopologues as a quantitative paleosalinity proxy. Paleoceanography 26. https://doi.org/10.1029/2010PA002043.
LeGrande, A.N., Schmidt, G.A., 2006. Global gridded data set of the oxygen isotopic composition in seawater. Geophys. Res. Lett. 33, L12604. https://doi.org/10.1029/2006GL026011.
Linsley, B.K., Rosenthal, Y., Oppo, D.W., 2010. Holocene evolution of the Indonesian throughflow and the western Pacific warm pool. Nat. Geosci. 3, 578–583.
Liu, Z., 2002. A simple model study of ENSO suppression by external periodic forcing. J. Clim. 15, 1088–1098. https://doi.org/10.1175/1520-0442(2002)015<1088:ASMSOE>2.0.CO;2.
Liu, Z., Kutzbach, J., Wu, L., 2000. Modeling climate shift of el nino variability in the Holocene. Geophys. Res. Lett. 27, 2265–2268.
Liu, Z., Lu, Z., Wen, X., Otto-Bliesner, B.L., Timmermann, A., Cobb, K.M., 2014. Evolution and forcing mechanisms of El Nino over the past 21,000 years. Nature 515, 550–553.
Lohmann, G., Butzin, M., Eissner, N., Shi, X., Stepanek, C., 2020. Abrupt climate and weather changes across time scales. Paleoceanography and Paleoclimatology 35. https://doi.org/10.1029/2019PA003782 e2019PA003782.
Lough, J.M., 2004. A strategy to improve the contribution of coral data to high-resolution paleoclimatology. Palaeogeogr. Palaeoclimatol. Palaeoecol. 204, 115–143. https://doi.org/10.1016/S0031-0182(03)00727-2.
Luan, Y., Braconnot, P., Yu, Y., Zheng, W., 2015. Tropical Pacific mean state and ENSO changes: sensitivity to freshwater flux and remnant ice sheets at 9.5Â ka BP. Clim. Dynam. 1–18. https://doi.org/10.1007/s00382-015-2467-7.
Luan, Y., Braconnot, P., Yu, Y., Zheng, W., Marti, O., 2012. Early and mid-Holocene climate in the tropical Pacific: seasonal cycle and interannual variability induced by insolation changes. Clim. Past 8, 1093–1108. https://doi.org/10.5194/cp-8-1093-2012.
Maher, N., Milinski, S., Suarez-Gutierrez, L., Botzet, M., Dobrynin, M., Kornblueh, L., Kröger, J., Takano, Y., Ghosh, R., Hedemann, C., Li, C., Li, H., Manzini, E., Notz, D., Putrasahan, D., Boysen, L., Claussen, M., Ilyina, T., Olonscheck, D., Raddatz, T., Stevens, B., Marotzke, J., 2019. The Max Planck Institute grand ensemble: enabling the exploration of climate system variability. J. Adv. Model. Earth Syst. 11, 2050–2069. https://doi.org/10.1029/2019MS001639.
Masson-Delmotte, V., Schulz, M., Abe-Ouchi, A., Beer, J., Ganopolski, A., Jansen, E., Lambeck, K., Luterbacher, J., Naish, T., Osborn, T., 2013. Information from Paleoclimate Archives.
McCulloch, M., Mortimer, G., Esat, T., Xianghua, L., Pillans, B., Chappell, J., 1996. High resolution windows into early Holocene climate: Sr/Ca coral records from the Huon Peninsula. Earth Planet Sci. Lett. 138, 169–178.
McGregor, H.V., Fischer, M.J., Gagan, M.K., Fink, D., Phipps, S.J., Wong, H., Woodroffe, C.D., 2013a. A weak El Nino/Southern Oscillation with delayed seasonal growth around 4,300 years ago. Nat. Geosci. 6, 949–953.
McGregor, S., Timmermann, A., England, M.H., Elison Timm, O., Wittenberg, A.T., 2013b. Inferred changes in El Niño-Southern Oscillation variance over the past six centuries. Clim. Past 9, 2269–2284.
Mollier-Vogel, E., Leduc, G., Böschen, T., Martinez, P., Schneider, R.R., 2013. Rainfall response to orbital and millennial forcing in northern Peru over the last 18 ka. Quat. Sci. Rev. 76, 29–38.
Montaggioni, L.F., Le Cornec, F., Corrège, T., Cabioch, G., 2006. Coral barium/calcium record of mid-Holocene upwelling activity in New Caledonia, South-West Pacific. Palaeogeography, Palaeoclimatology. Palaeoecology 237, 436–455.
Moy, C.M., Seltzer, G.O., Rodbell, D.T., Anderson, D.M., 2002. Variability of el niño/southern oscillation activity at millenial timescales during the Holocene epoch. Nature 420, 162–165.
Otto-Bliesner, B.L., 1999. El Niño/La Niña and sahel precipitation during the middle Holocene. Geophys. Res. Lett. 26, 87–90.
Otto-Bliesner, B.L., Braconnot, P., Harrison, S.P., Lunt, D.J., Abe-Ouchi, A., Albani, S., Bartlein, P.J., Capron, E., Carlson, A.E., Dutton, A., Fischer, H., Goelzer, H., Govin, A., Haywood, A., Joos, F., LeGrande, A.N., Lipscomb, W.H., Lohmann, G., Mahowald, N., Nehrbass-Ahles, C., Pausata, F.S.R., Peterschmitt, J.-Y., Phipps, S.J., Renssen, H., Zhang, Q., 2017. The PMIP4 contribution to CMIP6 – Part 2: two interglacials, scientific objective and experimental design for Holocene and Last Interglacial simulations. Geosci. Model Dev. (GMD) 10, 3979–4003. https://doi.org/10.5194/gmd-10-3979-2017.
Otto-Bliesner, B.L., Brady, E.C., Shin, S.I., Liu, Z., Shields, C., 2003. Modeling El Niño and its tropical teleconnections during the last glacia-interglacial cycle. Geophys. Res. Lett. 30, 2198. https://doi.org/10.1029/2003GL018553.
Pausata, F.S.R., Zhang, Q., Muschitiello, F., Lu, Z., Chafik, L., Niedermeyer, E.M., Stager, J.C., Cobb, K.M., Liu, Z., 2017. Greening of the Sahara suppressed ENSO activity during the mid-Holocene. Nat. Commun. 8, 16020. https://doi.org/10.1038/ncomms16020.
Pirazzoli, P.A., Montaggioni, L.F., 1988. Holocene sea-level changes in French Polynesia. Palaeogeogr. Palaeoclimatol. Palaeoecol. 68, 153–175. https://doi.org/10.1016/0031-0182(88)90037-5.
Reick, C.H., Raddatz, T., Brovkin, V., Gayler, V., 2013. Representation of natural and anthropogenic land cover change in MPI-ESM. J. Adv. Model. Earth Syst. 5, 459–482. https://doi.org/10.1002/jame.20022.
Rein, B., 2007. How do the 1982/83 and 1997/98 El Niños rank in a geological record from Peru? Quat. Int. 161, 56–66.
Rodbell, D.T., Seltzer, G.O., Anderson, D.M., Abbott, M.B., Enfield, D.B., Newman, J.H., 1999. An ~15,000-year record of el nino driven alluviation in southwestern Ecuador. Science 283, 516–520.
Rodríguez-Morata, C., Díaz, H.F., Ballesteros-Canovas, J.A., Rohrer, M., Stoffel, M., 2019. The anomalous 2017 coastal El Niño event in Peru. Clim. Dynam. 52, 5605–5622. https://doi.org/10.1007/s00382-018-4466-y.
Russon, T., Tudhope, A.W., Collins, M., Hegerl, G.C., 2015. Inferring changes in ENSO amplitude from the variance of proxy records. Geophys. Res. Lett. 42, 1197–1204. https://doi.org/10.1002/2014GL062331.
Russon, T., Tudhope, A.W., Hegerl, G.C., Collins, M., Tindall, J., 2013. Inter-annual tropical Pacific climate variability in an isotope-enabled CGCM: implications for interpreting coral stable oxygen isotope records of ENSO. Clim. Past 9, 1543–1557. https://doi.org/10.5194/cp-9-1543-2013.
Sachs, J.P., Blois, J.L., McGee, T., Wolhowe, M., Haberle, S., Clark, G., Atahan, P., 2018. Southward shift of the pacific ITCZ during the Holocene. Paleoceanography and Paleoclimatology 33, 1383–1395. https://doi.org/10.1029/2018PA003469.
Sadekov, A.Y., Ganeshram, R., Pichevin, L., Berdin, R., McClymont, E., Elderfield, H., Tudhope, A.W., 2013. Palaeoclimate reconstructions reveal a strong link between El Niño-Southern Oscillation and Tropical Pacific mean state. Nat. Commun. 4 (2692). https://doi.org/10.1038/ncomms3692.
Saint-Lu, M., Braconnot, P., Leloup, J., Lengaigne, M., Marti, O., 2015. Changes in the ENSO/SPCZ relationship from past to future climates. Earth Planet Sci. Lett. 412, 18–24.
Sandweiss, D.H., Andrus, C.F.T., Kelley, A.R., Maasch, K.A., Reitz, E.J., Roscoe, P.B., 2020. Archaeological climate proxies and the complexities of reconstructing Holocene El Niño in coastal Peru. Proc. Natl. Acad. Sci. 117, 8271–8279. https://doi.org/10.1073/pnas.1912242117.
Sandweiss, D.H., McInnis, H., Burger, R.L., Cano, A., Ojeda, B., Paredes, R., Sandweiss, M.C., Glascock, M.D., 1998. Quebrada Jaguay: South American maritime adaptations. Science 281, 1830–1832.
Schmidt, G.A., Annan, J.D., Bartlein, P.J., Cook, B.I., Guilyardi, E., Hargreaves, J.C., Harrison, S.P., Kageyama, M., LeGrande, A.N., Konecky, B., Lovejoy, S., Mann, M.E., Masson-Delmotte, V., Risi, C., Thompson, D., Timmermann, A.,

Tremblay, L.B., Yiou, P., 2014. Using palaeo-climate comparisons to constrain future projections in CMIP5. Clim. Past 10, 221–250.
Schmitt, J., Schneider, R., Elsig, J., Leuenberger, D., Lourantou, A., Chappellaz, J., Köhler, P., Joos, F., Stocker, T.F., Leuenberger, M., Fischer, H., 2012. Carbon isotope constraints on the deglacial CO_2 rise from ice cores. Science 336 (711). https://doi.org/10.1126/science.1217161.
Schneider, T., Hampel, H., Mosquera, P.V., Tylmann, W., Grosjean, M., 2018. Paleo-ENSO revisited: Ecuadorian Lake Pallcacocha does not reveal a conclusive El Niño signal. Glob. Planet. Chang. 168, 54–66.
Sepulchre, P., Caubel, A., Ladant, J.-B., Bopp, L., Boucher, O., Braconnot, P., Brockmann, P., Cozic, A., Donnadieu, Y., Dufresne, J.-L., Estella-Perez, V., Ethé, C., Fluteau, F., Foujols, M.-A., Gastineau, G., Ghattas, J., Hauglustaine, D., Hourdin, F., Kageyama, M., Khodri, M., Marti, O., Meurdesoif, Y., Mignot, J., Sarr, A.-C., Servonnat, J., Swingedouw, D., Szopa, S., Tardif, D., 2020. IPSL-CM5A2 – an Earth system model designed for multi-millennial climate simulations. Geosci. Model Dev. (GMD) 13, 3011–3053. https://doi.org/10.5194/gmd-13-3011-2020.
Shulmeister, J., Lees, B.G., 1995. Pollen evidence from tropical Australia for the onset of an ENSO-dominated climate at c. 4000 B.P. Holocene 5, 10–18.
Sidorenko, D., Goessling, H.F., Koldunov, N.V., Scholz, P., Danilov, S., Barbi, D., Cabos, W., Gurses, O., Harig, S., Hinrichs, C., Juricke, S., Lohmann, G., Losch, M., Mu, L., Rackow, T., Rakowsky, N., Sein, D., Semmler, T., Shi, X., Stepanek, C., Streffing, J., Wang, Q., Wekerle, C., Yang, H., Jung, T., 2019. Evaluation of FESOM2.0 coupled to ECHAM6.3: preindustrial and HighResMIP simulations. J. Adv. Model. Earth Syst. 11, 3794–3815. https://doi.org/10.1029/2019MS001696.
Stein, K., Timmermann, A., Schneider, N., Jin, F.-F., Stuecker, M.F., 2014. ENSO seasonal synchronization theory. J. Clim. 27, 5285–5310. https://doi.org/10.1175/JCLI-D-13-00525.1.
Stephans, C.L., Quinn, T.M., Taylor, F.W., Corrège, T.C.L., 2004. Assessing the reproducibility of coral-based climate records. Geophys. Res. Lett. 31. https://doi.org/10.1029/2004GL020343.
Stevens, B., Giorgetta, M., Esch, M., Mauritsen, T., Crueger, T., Rast, S., Salzmann, M., Schmidt, H., Bader, J., Block, K., Brokopf, R., Fast, I., Kinne, S., Kornblueh, L., Lohmann, U., Pincus, R., Reichler, T., Roeckner, E., 2013. Atmospheric component of the MPI-M earth system model: ECHAM6. J. Adv. Model. Earth Syst. 5, 146–172. https://doi.org/10.1002/jame.20015.
Stevenson, S., McGregor, H.V., Phipps, S.J., Fox-Kemper, B., 2013. Quantifying errors in coral-based ENSO estimates: towards improved forward modeling of δ18O. Paleoceanography 28, 633–649. https://doi.org/10.1002/palo.20059.
Stevenson, S., Powell, B., Cobb, K.M., Nusbaumer, J., Merrifield, M., Noone, D., 2018. Twentieth century seawater δ18O dynamics and implications for coral-based climate reconstruction. Paleoceanography and Paleoclimatology 33, 606–625. https://doi.org/10.1029/2017PA003304.
Stocker, T., Qin, D., Plattner, G.-K., Tignor, M., Allen, S.K., Boschung, J., Nauels, A., Xia, Y., Bex, V., Midgley, P.M., 2013. Climate Change 2013: the Physical Science Basis. Cambridge University Press, Cambridge, UK, and New York.
Stott, P.A., Gillett, N.P., Hegerl, G.C., Karoly, D.J., Stone, D.A., Zhang, X., Zwiers, F., 2010. Detection and attribution of climate change: a regional perspective. WIREs Climate Change 1, 192–211. https://doi.org/10.1002/wcc.34.
Sulca, J., Takahashi, K., Espinoza, J.-C., Vuille, M., Lavado-Casimiro, W., 2018. Impacts of different ENSO flavors and tropical Pacific convection variability (ITCZ, SPCZ) on austral summer rainfall in South America, with a focus on Peru. Int. J. Climatol. 38, 420–435.
Takahashi, K., Martínez, A.G., 2019. The very strong coastal El Niño in 1925 in the far-eastern Pacific. Clim. Dynam. 52, 7389–7415. https://doi.org/10.1007/s00382-017-3702-1.
Takahashi, K., Montecinos, A., Goubanova, K., Dewitte, B., 2011. ENSO regimes: reinterpreting the canonical and modoki el Niño. Geophys. Res. Lett. 38. https://doi.org/10.1029/2011GL047364.
Taylor, K.E., Stouffer, R.J., Meehl, G.A., 2012. An overview of CMIP5 and the experiment design. Bull. Am. Meteorol. Soc. 93, 485–498. https://doi.org/10.1175/BAMS-D-11-00094.1.
Thompson, D.M., Ault, T.R., Evans, M.N., Cole, J.E., Emile-Geay, J., 2011. Comparison of observed and simulated tropical climate trends using a forward model of coral d18O. Geophys. Res. Lett. 38. https://doi.org/10.1029/2011GL048224.
Timmermann, A., Okumura, Y., An, S.-I., Clement, A., Dong, B., Guilyardi, E., Hu, A., Jungclaus, J.H., Renold, M., Socker, T.F., Souffer, R.J., Sutton, R., Xie, S.-P., Yin, J., 2007. The influence of a weakening of the Atlantic meridional overturning circulation on ENSO. J. Clim. 20, 4899–4919.
Tudhope, A.W., Chilcott, C.P., McCulloch, M.T., Cook, E.R., Chappell, J., Ellam, R.M., Lea, D.W., Lough, J.M., Shimmield, G.B., 2001. Variability in the el-niño southern oscillation through a glacial-interglacial cycle. Science 291, 1511–1517.
Tziperman, E., Cane, M.A., Zebiak, S.E., 1995. Irregularity and locking to the seasonal cycle in an ENSO prediction model as explained by the quasi-periodicity route to chaos. J. Atmos. Sci. 52, 293–306.
Tziperman, E., Cane, M.A., Zebiak, S.E., Xue, Y., Blumenthal, B., 1998. Locking of El Niño's peak time to the end of the calendar year in the delayed oscillator picture of ENSO. J. Clim. 11, 2191–2199.
Tziperman, E., Stone, L., Cane, M.A., Jarosh, H., 1994. El Niño chaos: overlapping of resonances between the seasonal cycle and the pacific ocean-atmosphere oscillator. Science 264, 72–74.
Vargas-Ángel, B., Huntington, B., Brainard, R.E., Venegas, R., Oliver, T., Barkley, H., Cohen, A., 2019. El niño-associated catastrophic coral mortality at jarvis island, central equatorial pacific. Coral Reefs 38, 731–741. https://doi.org/10.1007/s00338-019-01838-0.
Vorrath, M.-E., Müller, J., Rebolledo, L., Cárdenas, P., Shi, X., Esper, O., Opel, T., Geibert, W., Muñoz, P., Haas, C., Kuhn, G., Lange, C.B., Lohmann, G., Mollenhauer, G., 2020. Sea ice dynamics in the Bransfield Strait, Antarctic Peninsula, during the past 240 years: a multi-proxy intercomparison study. Clim. Past 16, 2459–2483. https://doi.org/10.5194/cp-16-2459-2020.
Wang, P., Clemens, S., Beaufort, L., Braconnot, P., Ganssen, G., Jian, Z., Kershaw, P., Sarntheim, M., 2005. Evolution and variability of the Asian monsoon system: state of the art and outstanding issues. Quat. Sci. Rev. 24, 595–629.
Welsh, K., Elliot, M., Tudhope, A., Ayling, B., Chappell, J., 2011. Giant bivalves (Tridacna gigas) as recorders of ENSO variability. Earth Planet Sci. Lett. 307, 266–270.
Williamson, M.S., Collins, M., Drijfhout, S.S., Kahana, R., Mecking, J.V., Lenton, T.M., 2018. Effect of AMOC collapse on ENSO in a high resolution general circulation model. Clim. Dynam. 50, 2537–2552. https://doi.org/10.1007/s00382-017-3756-0.
Wittenberg, A.T., 2009. Are historical records sufficient to constrain ENSO simulations? Geophys. Res. Lett. 36, L12702.
Woodroffe, S.A., Horton, B.P., 2005. Holocene sea-level changes in the Indo-Pacific. J. Asian Earth Sci. 25, 29–43. https://doi.org/10.1016/j.jseaes.2004.01.009.
Yan, H., Wei, W., Soon, W., An, Z., Zhou, W., Liu, Z., Wang, Y., Carter, R.M., 2015. Dynamics of the intertropical convergence zone over the western pacific during the little ice age. Nat. Geosci. 8, 315–320.
Yeh, S.-W., Kug, J.-S., Dewitte, B., Kwon, M.-H., Kirtman, B.P., Jin, F.-F., 2009. El Nino in a changing climate. Nature 461, 511–514.
Zhang, Z., Leduc, G., Sachs, J.P., 2014. El Niño evolution during the Holocene revealed by a biomarker rain gauge in the Galápagos Islands. Earth Planet Sci. Lett. 404, 420–434. https://doi.org/10.1016/j.epsl.2014.07.013.
Zheng, W., Braconnot, P., Guilyardi, E., Merkel, U., Yu, Y., 2008. ENSO at 6ka and 21ka from ocean-atmosphere coupled model simulations. Clim. Dynam. 30. https://doi.org/10.1007/s00382-007-0320-3.